

Polymerised superparamagnetic antigen presenting cell lymphocyte capture for enriching tumour reactive T-cells and neoantigen identification

Received: 5 May 2024

Accepted: 21 May 2025

Published online: 02 June 2025



Chung-Yao Hsu^{1,2}, Po-Cheng Tsai^{1,2}, Jung-Chen Lin^{2,3,4,5}, Chen-Hsueh Pai², Yun-Jui Teng⁶, Bing-Yu Yao², Cheng-Yin Fei^{1,2}, Gwo Harn Max Shiau², Leon CW Lin², Sean Lo², Hung-Chih Yang⁷✉ & Che-Ming Jack Hu^{1,2,8}✉

Ultrasensitive antigen recognition between T lymphocytes and cognate targets via immunological synapse (IS) formation enables live cell-based antigen-specific T cell detection. However, unpredictable antigen processing and major histocompatibility complex (MHC) turnover limit specificity. Here, intracellularly polymerized antigen-presenting cells (pAPCs) are developed for modular, persistent antigen display via kinetically driven loading. Although inanimate, pAPCs mimic cellular interactions, inducing IS hallmarks such as supramolecular activation cluster formation, cytoskeletal contraction, and trogocytosis. Incorporation of superparamagnetic nanoparticles allows label-free magnetic isolation of antigen-specific T cells, surpassing MHC-conjugated beads in sensitivity and specificity. In tumor-bearing hosts, pAPCs enrich tumor-reactive lymphocytes, enhancing adoptive T cell therapy and neoantigen-specific T cell identification. Additionally, pAPCs from engineered cells expressing monovalent human MHC enrich virus- and tumor-specific CD8 T cells from human peripheral blood mononuclear cells and human leukocyte antigen-transgenic mice, demonstrating the potential of this cell–gel hybrid platform for precise antigen-specific T cell capture.

Isolation of antigen-specific T lymphocytes have immense biomedical values in fundamental research and clinical development^{1–4}. On one hand, identification of antigen-specific T cell helps delineate the immunological landscape during disease progression^{5,6}. On the other, isolation of antigen-specific lymphocytes is routinely performed in preclinical and clinical development to enhance safety and

effectiveness of adoptive cell therapies^{7–11}. Despite continuing development of T cell capturing strategies, discriminating rare antigen-specific T cells in an endogenous setting remains challenging given the inherently low affinity between peptide MHC complexes (pMHC) and cognate T cell receptors (TCR) ($K_d = 10^{-4}$ to 10^{-6} M)^{12–14}. While capture probes with pMHC multimer conjugation are commonly adopted to

¹Taiwan International Graduate Student Program, National Yang Ming Chiao Tung University and Academia Sinica, Taipei, Taiwan, ROC. ²Institute of Biomedical Sciences, Academia Sinica, Taipei, Taiwan, ROC. ³Institute of Oral Tissue Engineering and Biomaterials, College of Dentistry, National Yang Ming Chiao Tung University, Taipei, Taiwan, ROC. ⁴Institute of Oral Biology, College of Dentistry, National Yang Ming Chiao Tung University, Taipei, Taiwan, ROC. ⁵Oral Medicine Innovation Center (OMIC), National Yang Ming Chiao Tung University, Taipei, Taiwan, ROC. ⁶Department of Biochemical Science and Technology, College of Life Science, National Taiwan University, Taipei, Taiwan, ROC. ⁷Graduate Institute of Microbiology, College of Medicine, National Taiwan University, Taipei, Taiwan, ROC. ⁸Center of Applied Nanomedicine, National Cheng Kung University, Tainan, Taiwan, ROC. ✉e-mail: hcyang88@ntu.edu.tw; chu@ibms.sinica.edu.tw

increase binding affinity against target T cells^{15–19}, concerns regarding probe specificity due to the fundamental tradeoff between sensitivity and specificity associated with passive probe designs has prompted growing development of live-cell based strategies for antigen-specific T cell identification^{17,20,21}. Efforts to exploit nature's active antigen recognition mechanism have inspired T cell identification strategies based on engineered cellular systems^{22–27}. Through genetic and chemical engineering of antigen presenting cells (APC), cell-based approaches have been designed to confer signals or cellular labels following lymphocyte contact with the live cell probes. Despite promising studies supporting utility of live cell probes for antigen-specific lymphocyte identification, their specificity can be limited by unpredictable antigen presentation as a result of stochastic antigen processing and continuous MHC turnover^{28–30}. In addition, cumbersome maintenance requirement of live cell probes further constrains their adoption and functionalization, thus presenting fundamental challenges towards leveraging cell-like pMHC-TCR engagement dynamics for lymphocyte isolation.

In nature, the intricate balance between sensitivity and specificity in T cell engagement is achieved through the formation of immunological synapse (IS), which establishes stable and prolonged contact in the presence of weak pMHC-TCR interactions. This biological phenomenon is triggered by a serial process involving receptor clustering, co-stimulator signaling, and actin cytoskeleton remodeling that selectively recognize and amplify weak interaction events^{31–34}. Recently, cytosolically polymerized cells prepared from our and others' laboratories have shown the feasibility to stabilize cell membrane proteins in inanimate cell-gel hybrids for cognate ligand interactions^{35–39}. However, whether the polymerization strategy can preserve the biomembrane interface for bona fide IS engagement remains unknown. Herein, we demonstrate polymer-stabilized antigen presenting cells (pAPCs) faithfully retain the biomembrane interface for IS formation with cognate T cells, thereby enabling development of robust, stable probes for biomimetic lymphocyte capture. Functionalizability of pAPCs is demonstrated through the incorporation of superparamagnetic nanoparticles, which facilitates label-free, magnetic isolation of antigen-specific T lymphocytes. As polymer-stabilization deprives pAPCs of MHC turnover, controllable and persistent antigen presentation can be achieved following kinetically driven peptide antigen loading.

Here, we show that interaction between pAPCs and cognate T cells lead to stable IS formation as evidenced by the manifestation of supra-molecular activation clusters (SMACs), cytoskeletal remodeling within engaged T cells, and occurrence of trogocytosis. Notably, the biomimetic lymphocyte engagement can be observed on pAPCs stored under lyophilization for 6 months, thus enabling prolonged and practical utility of the biomimetic capture probe. The stabilized pAPCs enable systematic examination of IS-mediated lymphocyte capture at varying cellular incubation densities and incubation time, and it allows for direct comparison between IS-mediated lymphocyte capture and conventional passive probes based on pMHC-functionalized beads. pAPCs are further shown to enhance anticancer adoptive T cell therapy and improve detection of neoantigen-specific T cells upon lymphocyte isolation from tumor-burdened hosts. Lastly, pAPCs prepared with genetically engineered HEK 293 T cells displaying monoallelic human leukocyte antigen HLA-A*0201 is demonstrated. The HLA-expressing pAPCs functionalized with target antigens effectively enrich tumor-specific T cells from HLA-transgenic transgenic mice and virus-specific T cells from human peripheral blood mononuclear cells (PBMCs), providing a clinically applicable strategy for rare lymphocyte isolation and identification.

Results

Preparation of magnetized pAPCs with preserved biomembrane interface

Cytosolic polymerization of APCs was achieved through a rapid, non-disruptive photochemistry using a membrane-permeable low-

molecular-weight polyethyleneglycol-diacrylate monomer (575 Da) and a blue-light-sensitive lithium phenyl-2,4,6-trimethylbenzoylphosphine (LAP) photoinitiator^{35,36}. To bestow pAPC magnetic properties for label-free T cell isolation, APCs were incorporated with superparamagnetic nanoparticles prior to polymerization. A JAWSII dendritic cell line was first activated by LPS, and its magnetization was achieved through cellular engulfment of magnetic nanoparticles (Fig. 1A, B). The adoption of 60 nm PEGylated superparamagnetic iron oxide nanoparticles (SPION) (Supplementary Fig. 1A) led to efficient generation of aggregation-free, monodisperse magnetic pAPCs that undergo efficient clustering and dispersion in the presence and absence of a magnetic field, respectively (Supplementary Fig. 1B). While cytosolic polymerization yielded constructs morphologically identical to live dendritic cells, polymer-mediated structural stabilization was manifested upon placing pAPCs and live cells into hypotonic solutions (water), in which pAPCs were resistant to the osmotic change (Fig. 1C). Magnetization of the pAPCs were first confirmed by transmission electron microscopy (TEM), which revealed a high abundance of SPION inside the pAPCs (Fig. 1D). Assessment by magnetically induced clustering further showed that 80% of the freshly prepared pAPCs were superparamagnetic (Supplementary Fig. 1C), and a single washing step to remove non-magnetized pAPCs led to 100% magnetized pAPCs for subsequent lymphocyte capture (Fig. 1E, F). The presence of surface proteins responsible for lymphocyte engagement and IS formation, including MHC, CD80, CD86, and intercellular adhesion molecule 1 (ICAM-1), was further confirmed by flow cytometric analysis, which showed that reconstituted pAPCs possessed identical lymphocyte activation molecules to live APCs (Fig. 1G). Cytosolic polymerization conferred robust stability for prolonged storage as reconstituted pAPCs following 6 months of storage by lyophilization maintained all the signaling molecules associated with IS formation (Fig. 1H, I, Supplementary Fig. 1D). All subsequent experiments were performed with reconstituted pAPCs following lyophilization and were verified to be free of endotoxin content before use (Supplementary Fig. 1E).

Kinetically driven peptide replacement enables modular and persistent antigen presentation by pAPCs

To modulate pAPCs' antigen presentation to desired peptide targets, we adopted a kinetically driven peptide replacement approach by subjecting pAPCs to antigen of choice at concentrations above the peptide's dissociation constant (Fig. 2A). Using SIINFEKL as a model antigen, antigen replacement on pAPCs was accomplished in a concentration-dependent fashion (Fig. 2B and Supplementary Fig. 2A). Evaluation of SIINFEKL presentation on the pAPCs through SIINFEKL/H-2kb antibody staining showed that antigen replacement positively correlated with the extracellular peptide concentration, and at 2 mg/mL SIINFEKL complete antigen replacement was achieved within 1 min (Fig. 2C). To compare antigen presentation on pAPCs to live cell probes, we prepared live APCs with commonly adopted antigen delivery approaches, including incubation with antigen-containing protein, incubation with long peptides, transfection with antigen-containing plasmid, and short peptide pulsing (Fig. 2D, E). In comparison to pAPCs following antigen replacement, live APCs following incubation or transfection with proteins, long peptides, or plasmids containing SIINFEKL sequence showed subdued SIINFEKL/H-2kb signals, which reflected antigen processing inefficiency that could influence probe specificity. Direct pulsing of live APCs with SIINFEKL peptides resulted in comparable antigen presentation as antigen-loaded pAPCs. However, MHC turnover of live cells led to a rapid decline in surface antigen presentation (Fig. 2F and Supplementary Fig. 2B), whereas pAPCs allowed for controllable and persistent antigen presentation. To demonstrate the tailorability of pAPCs with peptide antigens of varying MHC binding affinities, we examined two other H-2kb-restricted peptides, PB1_{703–711} derived from influenza PB1 polymerase and E6_{48–57} derived from human papillomavirus E6

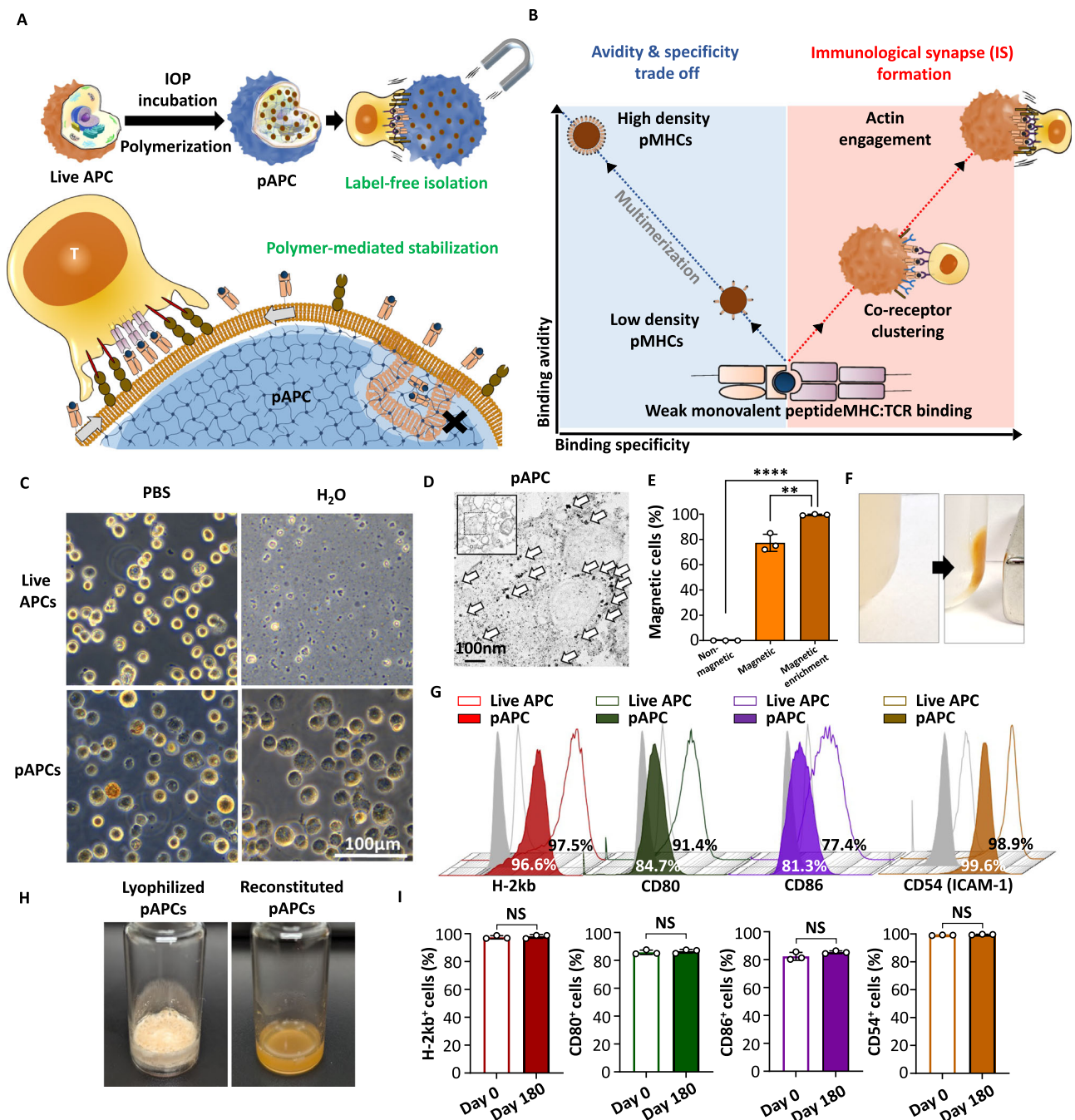


Fig. 1 | Preparation and characterization of magnetized pAPCs. **A** A schematic illustrating the preparation of magnetized polymerized antigen-presenting cells (pAPCs) and their attributes for immunological synapse-mediated antigen-specific T cell capture. Created in BioRender. Chen, H. (2025) <https://BioRender.com/qyctluu> **B** A schematic illustrating the binding affinity and binding specificity relationship for T cell engagement the passive probes containing multimeric ligands or with cellular targets through immunological synapse formation. **C** Bright-field microscopic observations of live JAWSII and magnetized pAPCs under isotonic buffer (PBS) and hypotonic buffer (water). Scale bar = 100 μ m. The experiment was independently repeated three times. **D** Transmission electron microscopy images showing the presence of iron-oxide nanoparticles in pAPCs. Arrows indicate the iron-oxide nanoparticles in the cytoplasm. The experiment was independently repeated three times. Scale bar = 100 nm. **E** Quantification of magnetized pAPCs

immediately following preparation and following a single round of magnetic enrichment. The error bars represent mean \pm standard deviation. P values from top to bottom, **** $p < 0.0001$, ** $p = 0.0049$ (Independent biological replicates $n = 3$). **F** Images showing pAPCs undergoing magnetically induced clustering. **G** Examination of surface proteins, including H-2kb, CD80, CD86, and ICAM1 on live APC and pAPCs by flow cytometric analysis. Hollow and solid gray histograms indicate isotype controls with live APCs or pAPCs, respectively. **H** Images showing lyophilized and water-reconstituted pAPCs. **I** Flow cytometric examination of surface proteins, including H-2kb, CD80, CD86, and ICAM1 on pAPCs following 180 days of storage by lyophilization. The error bars represent mean \pm standard deviation. P values from left to right. NS $p = 0.5630$, NS $p = 0.5588$, NS $p = 0.1688$, NS $p = 0.0657$ (Independent biological replicates $n = 3$). Statistical analyses were performed by two-sided Student's t tests.

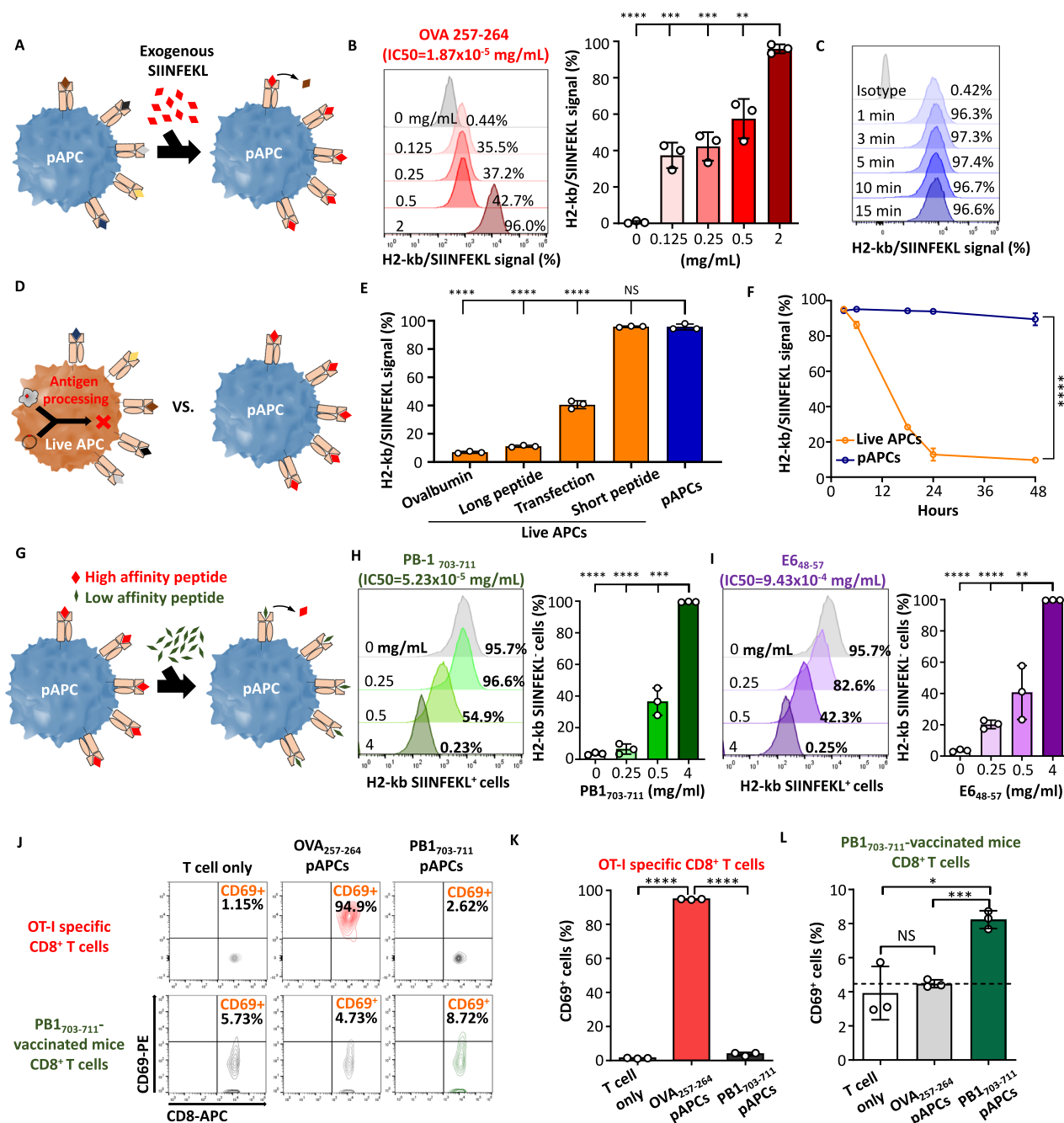


Fig. 2 | Modular antigen presentation on pAPCs through kinetically driven peptide replacement. **A** A Schematic illustrating the exogenous peptide exchange process. **B** The percentage of H2-kb-SIINFEKL⁺ pAPCs following incubation in various concentrations of SIINFEKL for 5 min. P values from left to right, **** $p < 0.0001$, *** $p = 0.0002$, ** $p = 0.0003$, ** $p = 0.0039$ (Independent biological replicates $n = 3$). **C** Flow cytometric analysis of H2-kb-SIINFEKL⁺ pAPCs following incubation with 2 mg/mL SIINFEKL at incubation time from 1 to 15 min. **D** A schematic illustrating antigen presentation by live APCs or pAPCs following antigen pulsing. **E** Live APCs were pulsed with ovalbumin, OVA₂₄₈₋₂₇₄ (27 amino acids), or SIINFEKL peptide for 4 h. For transfection, live APCs were transfected with SIINFEKL-containing plasmid for 48 h. Each group underwent flow cytometric analysis to characterize H2-kb-SIINFEKL⁺ cells. P values from left to right, **** $p < 0.0001$, **** $p < 0.0001$, **** $p < 0.0001$, NS $p = 0.8382$ (Independent biological replicates $n = 3$). **F** SIINFEKL antigen presentation over a 48 h period for SIINFEKL-pulsed live APC and SIINFEKL-loaded pAPCs. Live APCs were pulsed with 1 μ g/mL of SIINFEKL for 4 h and pAPCs were incubated with 2 mg/mL of SIINFEKL for 5 min prior to incubation. P values, **** $p < 0.0001$ (Independent biological replicates $n = 3$). **G** A schematic illustrating

the experimental design for assessing peptide exchange efficiency on pAPCs with MHC binders of low binding affinity. pAPCs were pre-loaded with SIINFEKL as a model strong binder. The extent of SIINFEKL peptide replacement upon incubation with various concentration of **H** PB1₇₀₃₋₇₁₁ or **I** E6₄₈₋₅₇ peptides. The replacement efficiency was determined by the proportion of H2-kb-SIINFEKL⁺ cells. P values in (**H**) from left to right, **** $p < 0.0001$, **** $p < 0.0001$, **** $p < 0.0002$. P values in (**I**) from left to right, **** $p < 0.0001$, **** $p < 0.0001$, ** $p = 0.004$ (Independent biological replicates $n = 3$). **J–L** Validation of pAPC antigen presentation through a T cell activation assay via flow cytometric analysis of CD69 levels. OT-I specific T cells derived from OT-I transgenic mice and splenocytes derived from PB1₇₀₃₋₇₁₁-vaccinated mice were incubated with SIINFEKL-loaded pAPCs or pAPCs following PB1₇₀₃₋₇₁₁ peptide replacement for 24 h prior to analysis of T cell activation. P values in (**K**) from left to right, **** $p < 0.0001$, **** $p < 0.0001$. P values in (**L**) from top to bottom, * $p = 0.0106$, *** $p = 0.0003$, NS $p = 0.5813$ (Independent mice replicates $n = 3$). The error bars represent mean \pm standard deviation. Statistical analyses were performed by two-sided Student's t tests.

protein, with lower MHC binding affinity as compared to SIINFEKL. Whereas SIINFEKL has a binding affinity of 19.37 nM ($IC_{50} = 1.87 \times 10^{-5}$ mg/mL), PB1₇₀₃₋₇₁₁ and E6₄₈₋₅₇ have binding affinities at 44.25 nM ($IC_{50} = 5.23 \times 10^{-5}$ mg/mL) and 700.35 nM ($IC_{50} = 9.43 \times 10^{-4}$ mg/mL), respectively (Supplementary Fig. 2C). To investigate the peptides' exchange efficiency, SIINFEKL-loaded pAPCs were subjected to different concentrations of PB1₇₀₃₋₇₁₁ or E6₄₈₋₅₇ (Fig. 2G). Despite the high binding affinity of SIINFEKL, SIINFEKL/H-2Kb⁺ cells decreased proportionally with increasing concentrations of the replacement peptides, and complete peptide replacement was achieved following 5 min of peptide incubation at 4 mg/mL of either PB1₇₀₃₋₇₁₁ or E6₄₈₋₅₇ (Fig. 2H, I). Presentation of the low-affinity antigens was further confirmed by a CD8⁺ T cell activation assay using CD8 T cells derived from OT-I transgenic or PB1-vaccinated mice (Supplementary Fig. 2D, E). Whereas control pAPCs without peptide loading had no reactivity with OT-I specific T cells, SIINFEKL-loaded pAPCs significantly upregulated OT-I specific T cells activation (Supplementary Fig. 2F). SIINFEKL-loaded pAPCs following PB1₇₀₃₋₇₁₁ peptide replacement were deprived of their ability to activate OT-I specific T cells. In contrast, these pAPCs were capable of elevating CD69 levels in CD8 T cells derived from PB1₇₀₃₋₇₁₁-vaccinated mice (Fig. 2J–L), corroborating that the high-affinity SIINFEKL has been replaced by the low-affinity PB1₇₀₃₋₇₁₁. These results demonstrate pAPCs' versatility for tunable, persistent antigen presentation, even for subdominant antigens with low MHC binding affinity.

pAPCs establish stable IS interface with cognate T cells for magnetic isolation

To examine the engagement of pAPCs with cognate CD8 T cells, we performed fluorescence antibody staining to visualize putative membrane molecules responsible for the formation of supramolecular activation complex (SMAC), including intracellular adhesion molecule 1 (ICAM-1) and MHC-I located on APCs and T cell receptor Vα2 chain (TCR Vα2) and lymphocyte function-associated antigen 1 (LFA-1) located on CD8 T cells (Supplementary Fig. 3A). Upon fluorescence microscopic examination of SIINFEKL-loaded pAPCs and OT-I-specific CD8 T cells, we observed polarization of ICAM-1, MHC-I, TCR, and LFA-1 towards the interface between pAPCs and T cells, highlighting that pAPCs permit retrograde flow of membrane molecules for T cell-mediated ligand alignment. Zoomed-in visualization of the pAPC/T cell interface further revealed ring patterns indicative of the establishment of central SMAC (cSMAC) and peripheral SMAC (pSMAC)⁴⁰. Whereas the periphery of the interface is rich in ICAM-1 and LFA-1, the center core of the interface is enriched with MHC-I and TCR (Fig. 3A, D). Relative fluorescence quantification performed with Image J software shows the enrichment of the MHC-I Cy5 signal and ICAM-1 FITC signal, as well as the TCR Vα2-FITC signal and LFA-1 PE signal only at the interface between pAPCs and T cells (Fig. 3B, C, E, F), indicating the formation of SMAC during engagement. As SMAC formation is governed by the molecular movement mediated by cytoskeleton movement within T cells, we also observed filamentous-actin (F-actin) within CD8 T cells through phalloidin staining. pAPC-engaged T cells showed polarized cytoskeletal remodeling supported by relative fluorescence enriched in phalloidin at the cell-cell interface (Fig. 3G, H), conferring contractile forces that strengthened pAPC binding. To demonstrate that the IS formation provides stable bonding amenable to magnetic isolation of cognate T cells, pAPCs incubated with OT-I T cells were subjected to a magnetic field. Time-lapse imaging revealed that the binding between T cells and pAPCs withstood the fluid shear under the magnetically induced movement (Fig. 3I). In addition, following extended incubation of fluorophore-conjugated pAPC and cognate T cells, we observed trogocytosis as active transfer of membrane molecules from pAPCs to T cells was detected (Supplementary Fig. 3B–D). Evidence of active membrane extraction by the T cells further corroborated bona fide IS formation and active bonding

between pAPCs and T cells. To further compare the engagement dynamics between pAPCs and live APCs with cognate T cells, we fluorescently labeled SIINFEKL-peptide loaded APCs (ICMA-1; green) and OT-I T cells (LFA-1; red) and monitored for engagement events (yellow) under imaging cytometry (Fig. 3J). The study showed comparable APC-T cell engagement dynamics between live APCs and pAPCs over a 3-h incubation period, whereas glutaraldehyde-fixed APCs and non-peptided loaded pAPCs showed minimal engagement events with OT-I T cells (Fig. 3K). Together, these results demonstrate the cell-like ability of pAPCs to establish IS for efficient capture and isolation of cognate T cells.

pAPCs enable systematic examination of cognate and non-cognate lymphocyte engagement

As lymphocyte engagement is a kinetic proofreading process that involves differential on/off-rates for non-cognate and cognate cellular interactions^{31,32}, the stabilized nature of pAPCs allows for systematic examination of cognate and non-cognate lymphocyte engagement (Fig. 4A). To represent non-cognate and cognate T cells, CD8⁺ T cells were derived from WT mouse and OT-I transgenic mice respectively. The WT mouse-derived T cells were stained with CFSE, whereas the T cells derived from OT-I mouse were left unstained for flow cytometric differentiation. The cognate and non-cognate CD8⁺ T cells were incubated at a 1–9 cellular ratio, and the ability of peptide-pulsed pAPCs for antigen-specific CD8⁺ T cell capture was first confirmed by adding magnetized pAPCs with or without SIINFEKL peptide pulsing for magnetic isolation (Fig. 4B and Supplementary Fig. 4A, B). In a time-course study with varying cellular incubation durations, we observed that IS-mediated T cell capture increased with incubation time during the first hour and reached a plateau between 1 and 6 h (Fig. 4C–F and Supplementary Fig. 4C). Incubation time below 1 h resulted in reduced cognate T cell recovery, which indicates inadequate incubation duration for IS establishment. The overall increase in T cell capture efficiency and the ensuing plateau coincided with the engagement kinetics observed in Fig. 3J. Notably, incubation beyond the 6 h mark reduced cognate T cell capture, and at the 36 h mark pAPCs were deprived of their T cell capture ability entirely. The decline in T cell capture capacity was presumably due to the trogocytosis phenomenon as a result of the robust engagement between pAPCs and cognate T cells, which led to the progressive loss of MHC-I molecules from the pAPCs upon prolonged incubation (Supplementary Fig. 3C). Adopting 2 h incubation time as the optimal condition upon considering both capture efficiency and enrichment fold, we then examined how cellular density may influence the IS engagement dynamic. Upon examining cellular densities between 0.125×10^6 to 2×10^6 cells/cm² (~15% confluency to 200% confluency), non-linear dynamics in capture yield and specificity were observed. As the cellular density increased from 0.125×10^6 cells/cm² to 0.25×10^6 cells/cm², an elevation in the recovery yield and enrichment fold of cognate T cells reflects enhanced collisional frequency favoring IS establishment between pAPCs and T cells for subsequent capture. Further increase in cellular density beyond 0.5×10^6 cells/cm², however, led to a reduction in capture specificity (Fig. 4G–J and Supplementary Fig. 4D, E). At cellular densities above 1×10^6 cells/cm², higher cellular crowding was associated with increasing capture of non-cognate T cells, although the recovery yield of cognate T cells remained superior. As non-cognate T cells are known to disengage from cellular targets at a faster rate than cognate T cells³², we further examined if non-cognate cellular dislodgement following T cell capture may enhance capture specificity for antigen-specific T cells (Fig. 4K). Based on the capture parameter of 0.25×10^6 cells/cm² and 2 h of incubation, pAPC capture followed by non-cognate dislodgement significantly increased the purity of cognate T cells in the isolation pool, increasing the enrichment fold by nearly 2 times and achieving a cognate T cell purity of ~80% (Fig. 4L). We further observed that pAPCs under prolonged storage (180 days) exhibited comparable

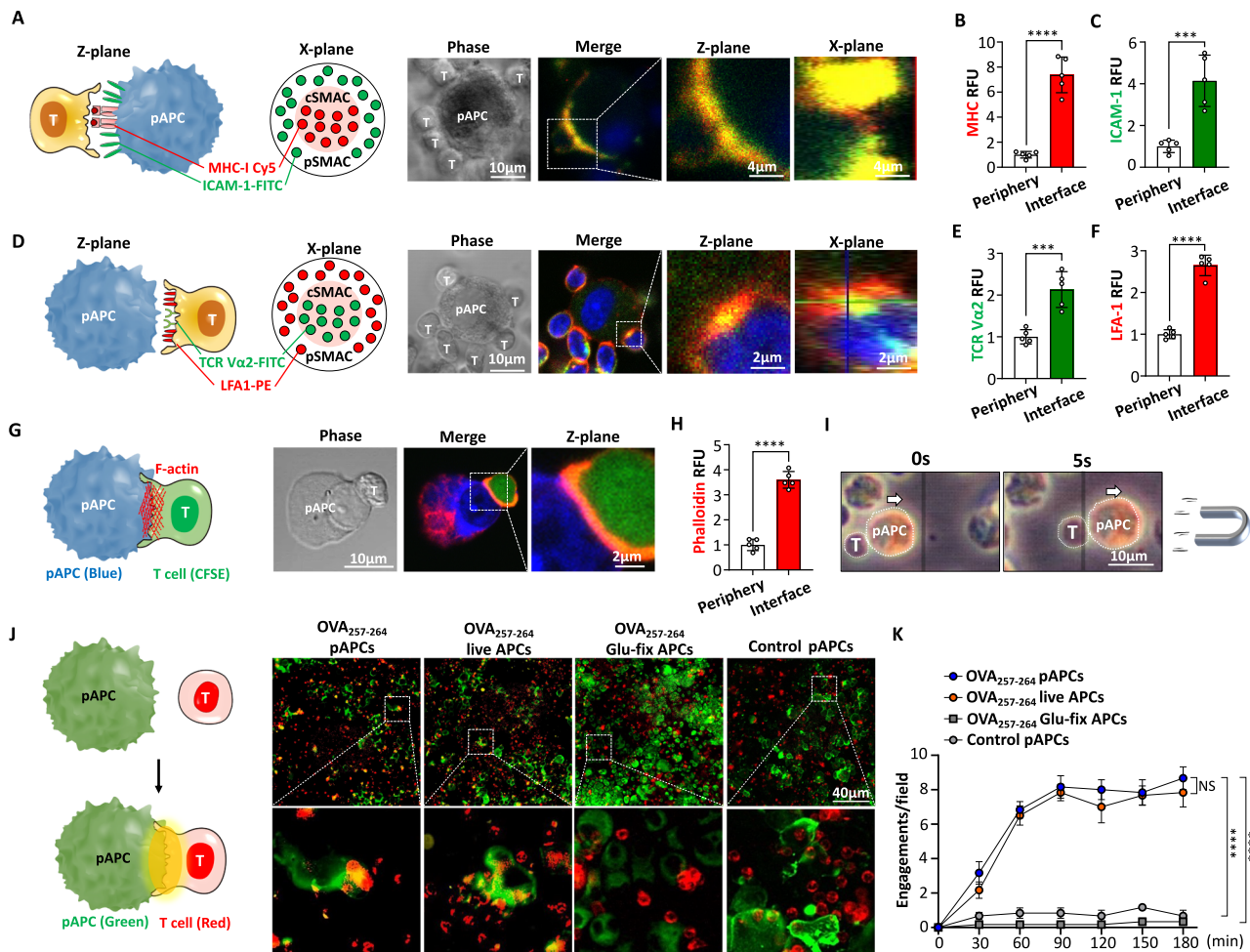


Fig. 3 | Immunological synapse formation between pAPCs and cognate T cells.

A Schematic illustration of polarized MHC-I and ICAM-1 distributions on APCs at the APC/T cell interface and fluorescence microscopy images showing patterned MHC-I and ICAM-1 distributions on pAPCs. The experiment was independently repeated two times. Scale bars = 10 and 4 μm . **B** Relative MHC fluorescence intensities and **C** ICAM-1 fluorescence intensities at the cellular contact interface and peripheral regions away from cellular contact are quantified. P value **** p < 0.0001 in (**B**) and *** p = 0.0005 in (**C**) (Independent biological replicates n = 5). **D** Schematic illustration of polarized TCR and LFA-1 distributions on T cells at the APC/T cell interface and fluorescence microscopy images showing patterned TCR and LFA-1 distributions on pAPC-engaged T cells. The experiment was independently repeated two times. Scale bars = 10 and 2 μm . **E** Relative TCR fluorescence intensities and **F** LFA-1 fluorescence intensities at the cellular contact interface and peripheral regions away from cellular contact are quantified. P value in *** p = 0.0006 in (**E**) and **** p < 0.0001 in (**F**) (Independent biological replicates n = 5). **G** OT-I CD8⁺ T cells

engaging with SIINFEKL-loaded pAPCs exhibit F-actin polarization at the cell-cell interface. The experiment was independently repeated two times. Scale bars = 10 and 2 μm . **H** Relative phalloidin intensities at the cellular contact interface and peripheral regions away from cellular contact are quantified. P value **** p < 0.0001 (Independent biological replicates n = 5). **I** Time-lapse microscopy images showing magnetized pAPC carrying engaged T cells upon magnetically induced movement. Arrows indicate the movement direction of pAPCs. Scale bar = 10 μm . **J** Schematic illustration of imaging cytometry analysis of APC/T cell engagement and representative fluorescence microscopy images of APC/T cell engagement events taken after 2 h of incubation. White arrows indicate engagement events. The experiment was independently repeated six times. Scale bar = 40 μm . **K** Kinetic analysis of engagement events over a 3 h incubation period. P values from left to right, NS = 0.4530, **** p < 0.0001, **** p < 0.0001 (Independent biological replicates n = 6). The error bars represent mean \pm standard deviation. Statistical analyses were performed by (**B**, **C**, **E**, **F**, **H**) two-sided Student's t tests and (**K**) one-way ANOVA.

biomimetic lymphocyte engagement and capture efficiency as freshly prepared pAPCs (Supplementary Fig. 5A–G). These results highlight the durable, cell-mimicking characteristics of pAPCs for antigen proofreading and provide optimal parameters for pAPC-mediated cellular capture.

pAPCs enable comparison of biomimetic lymphocyte capture to conventional pMHC-functionalized probes

The ability of magnetized pAPCs to isolate lymphocytes further allows for direct comparison of the biomimetic lymphocyte capture strategy to conventional passive magnetic beads. To compare pAPCs to conventional capture beads, we prepared dynabeads functionalized with various densities of SIINFEKL-H-2Kb monomer (2 – 2×10^4 pMHCs/ μm^2) for OT-I specific CD8⁺ T cell capture (Fig. 5A). Of note, pAPCs are presumed to have an average surface pMHC

density as live APCs (2×10^3 pMHCs/ μm^2)^{41,42}. Functionalization of streptavidin-conjugated dynabeads with biotinylated-SIINFEKL-H2Kb monomer resulted in surface pMHC presentation on the dynabeads as confirmed by immunofluorescence-mediated flow cytometric analysis (Fig. 5B), and protein quantification via a microBCA assay further confirmed quantitative control over the pMHC functionalization, yielding dynabeads with adjust surface pMHC densities up to 50×10^4 pMHCs per a $2.8 \mu\text{m}$ bead (2×10^4 pMHCs/ μm^2) (Fig. 5C). pAPCs' capture efficiency with various pMHC-coated beads were then compared in a CD8⁺ T cell pool containing 10% of OT-I T cells and 90% of non-cognate T cells derived from WT mice. Using dynabeads and pAPCs of comparable total surface areas, direct magnetic capture following 2 h of incubation showed that increasing pMHC density on dynabeads led to higher recovery of total CD8⁺ T cells, and dynabeads with 6×10^3 and 2×10^4 pMHCs/ μm^2 recovered higher

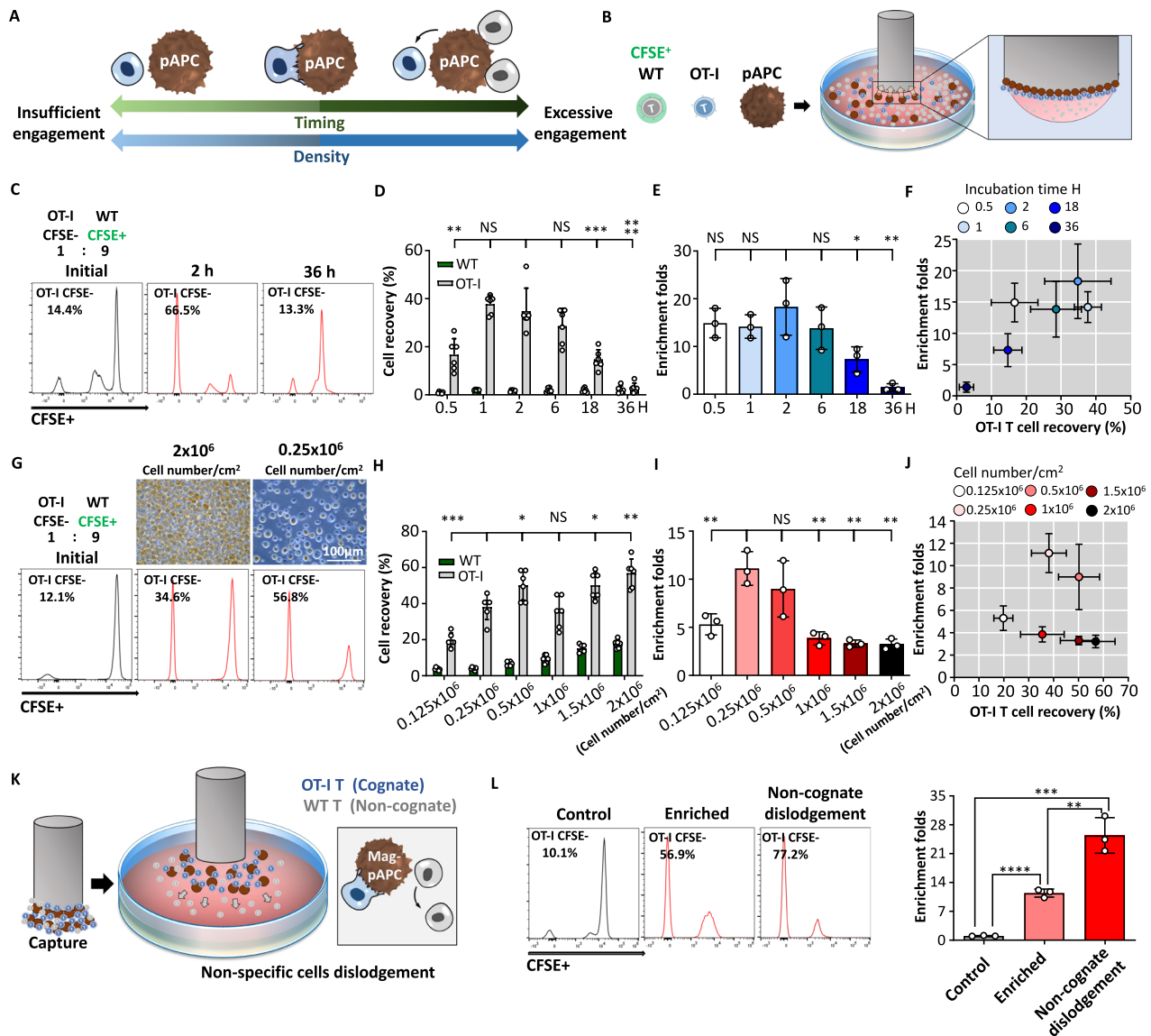


Fig. 4 | Examination of cognate T cell engagement by pAPCs. **A** Schematic illustration of parameters relevant to IS-mediated T cell capture. **B** Schematic illustration of device design and experimental setup for evaluating T cell capture with magnetized pAPCs. WT CD8⁺ T cells were differentiated from cognate, OT-I T cells through CFSE staining. Magnetic capture was achieved with a parafilm-wrapped magnet, and captured cells were isolated through parafilm removal. **C** Representative flow cytometric histogram demonstrating enrichment of antigen-specific CD8⁺ T cells following magnetic isolation by pAPCs upon 2 h of incubation. 10^6 CD8⁺ T cells containing 10% of OT-I CD8⁺ T cells were incubated with 10^6 pAPCs. T cells and pAPCs were incubated from 0.5 h to 36 h then prior to magnetic isolation and flow cytometric analysis. **D** OT-I and WT T cell recovery rate (%) (Independent biological replicates $n = 6$) and **E**, **F** OT-I CD8⁺ T enrichment fold were calculated based on pre-capture and post-capture OT-I/WT CD8⁺ T cell numbers (Independent biological replicates $n = 3$). *P* values in (**D**) from left to right, $^{**}p = 0.0034$, $NS\ p = 0.5096$, $NS\ p = 0.2303$, $^{***}p = 0.0008$, $^{****}p < 0.0001$. *P* values in (**E**) from left to right, $NS\ p = 0.4303$, $NS\ p = 0.3302$, $NS\ p = 0.3564$, $^*p = 0.0431$, $^{**}p = 0.0082$. **G** Representative flow cytometric histogram demonstrating enrichment of antigen-specific CD8⁺ T cells following magnetic isolation by pAPCs upon

cellular incubation at 0.25×10^6 cellular density. 10^6 of T cells with 10% of OT-I T cells were incubated with 10^6 pAPCs for 2 h prior to isolation and flow cytometric analysis. The influence of cellular incubation densities on cognate T cell capture was assessed based on a 2 h incubation time. The experiment was independently repeated three times. **H** OT-I and WT T cell recovery rate (%) (Independent biological replicates $n = 6$) and **I**, **J** OT-I CD8⁺ T enrichment fold were calculated based on pre-capture and post-capture OT-I/WT CD8⁺ T cell numbers (Independent biological replicates $n = 3$). *P* values in (**H**) from left to right, $^{***}p = 0.0002$, $^{**}p = 0.021$, $NS\ p = 0.5745$, $^*p = 0.0162$, $^{**}p = 0.0014$. *P* values in (**I**) from left to right, $^{**}p = 0.0082$, $NS\ p = 0.3403$, $^{**}p = 0.0026$, $^{**}p = 0.0016$, $^{**}p = 0.0017$. **K** Schematic illustration of pAPCs-captured T cells subjected to 15 min of non-cognate cellular dislodgement. **L** Enrichment fold of OT-I T cells after pAPC-mediated capture and pAPC-mediated capture with dislodgement treatment. *P* values from top to bottom, $^{***}p = 0.0006$, $^{**}p = 0.0054$, $^{****}p < 0.0001$ (Independent biological replicates $n = 3$). Three or six independent experiments were conducted ($n = 3$ or 6). The error bars represent mean \pm standard deviation. Statistical analyses were performed by two-sided Student's *t* tests.

numbers of total T cells than the SIINFELK-functionalized pAPCs (Fig. 5D). Analysis of OT-I specificity in the recovered T cells showed a saturation of cognate T cell recovery by pAPC and dynabeads with 2×10^3 , 6×10^3 , and 2×10^4 pMHCs/ μm^2 (Fig. 5E and Supplementary Fig. 6A, B). These results show that for passive capture probes, pMHC functionalization beyond an optimal density leads to non-specific

engagement with non-cognate T cells. Strikingly, 2×10^4 pMHCs/ μm^2 dynabeads failed to differentiate cognate and non-cognate T cells despite having a high total T cell recovery (Fig. 5F). On the other hand, pAPCs outperformed all dynabeads in overall enrichment in cognate T cells. In another T cell capture study in which cognate T cells were reduced to 0.1% of the total CD8⁺ T cell pool, the trade-

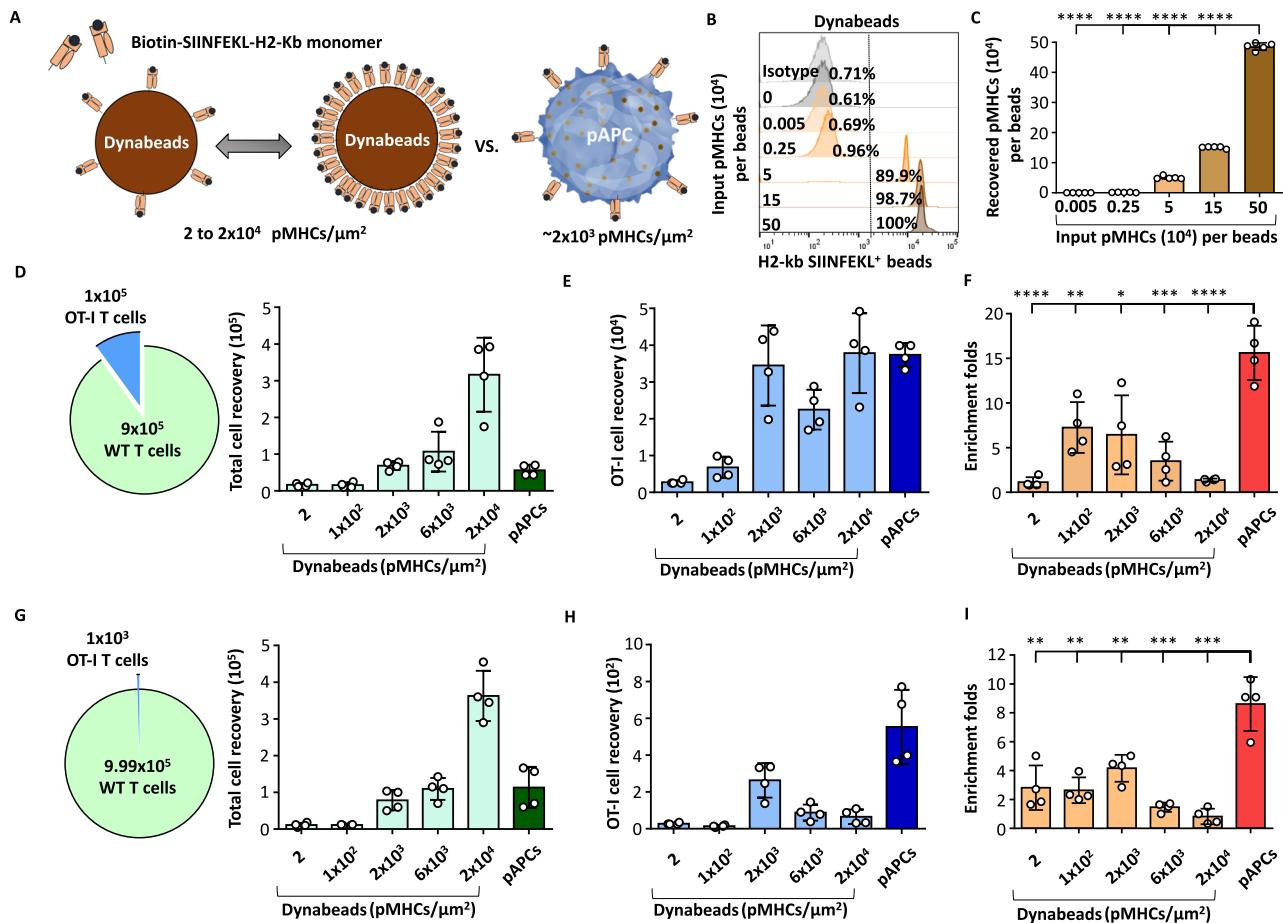


Fig. 5 | pAPCs obviate avidity-specificity trade-off associated with pMHC-functionalized capture probes. **A** Schematics illustrating dynabeads functionalized with varying pMHC densities ($2\text{--}2 \times 10^4$ pMHCs/ μm^2) and pAPC. **B** Flow cytometric characterization of streptavidin-functionalized dynabeads conjugated with different densities of biotin-SIINFEKL-H2Kb monomers using anti-H2-kb-SIINFEKL antibodies. **C** Protein quantification characterizing pMHC content on dynabeads using micro BCA assay. *P* values, *****p* < 0.0001 (Independent biological replicates *n* = 5). **D** Examination of T cell recovery by different capture probes in a CD8⁺ T cell pool containing 10% of cognate T cells. 10^6 T cells containing 10^5 OT-I T cells were incubated with 10^6 pAPCs or 5×10^7 dynabeads of equivalent total surface area for 2 h prior to T cell isolation and enumeration (Independent biological replicates *n* = 4). **E** Quantification of OT-I T cells recovery by the different capture probes (Independent biological replicates *n* = 4).

F Enrichment fold for cognate OT-I T cells following pAPC or dynabeads isolation. *P* value from left to right, *****p* < 0.0001 ***p* = 0.007, **p* = 0.0141, ****p* = 0.0006, *****p* = 0.0001 (Independent biological replicates *n* = 4). **G** Examination of T cell recovery by different capture probes in a CD8⁺ T cell pool containing 0.1% of cognate T cells. 10^6 T cells containing 10^3 OT-I T cells were incubated with 10^6 pAPCs or 5×10^7 dynabeads of equivalent total surface area for 2 h prior to T cell isolation and enumeration (Independent biological replicates *n* = 4). **H** Quantification of OT-I T cells recovery by the different capture probes (Independent biological replicates *n* = 4). **I** Enrichment fold for cognate OT-I T cells following pAPC or dynabeads isolation. *P* value from left to right, ***p* = 0.0031, ***p* = 0.0012, ***p* = 0.0053, ****p* = 0.0003, ****p* = 0.0002 (Independent biological replicates *n* = 4). The error bars represent mean \pm standard deviation. Statistical analyses were performed by two-sided Student's *t* tests.

off between affinity and specificity for passive capture probe was further amplified. The higher total T cell capture by high pMHC density dynabeads was contrasted by lower recovery of cognate OT-I T cells (Fig. 5G, H). In comparison, T cell capture by pAPCs recovered the most OT-I T cells with the least non-specific binding, resulting in the highest enrichment fold of OT-I T cells (Fig. 5I). Further examination of pMHC-functionalized dynabeads with varying bead concentrations did not improve cognate T cell enrichment (Supplementary Fig. 6C–J), and the results consistently reflected the specificity-avidity trade-off associated with passive probe design. These findings corroborated the advantage of biomimetic lymphocyte capture by pAPCs and highlighted its applicability for isolating lymphocyte targets of low abundance.

pAPC-mediated isolation of tumor-specific T cells enhances adoptive T cell therapy and neoantigen identification

Leveraging the superior lymphocyte capture efficiency by pAPCs, we further examined its applicability for isolating tumor-reactive T cells in

an endogenous setting. To generate endogenous tumor-reactive T cells in tumor-bearing hosts, we subcutaneously inoculated E.G7-OVA cells, followed by immune checkpoint blockade treatment (Supplementary Fig. 7A). The mice were then sacrificed and their spleens were collected for CD8⁺ T cells isolation with SIINFEKL-loaded pAPCs and pMHC-functionalized Dynabeads (Fig. 6A). FACS analysis reveals that direct capture by pAPCs on tumor-burdened hosts consistently enriched OVA_{257–264}-specific T cells, yielding an overall enrichment fold of ~300%. However, capturing with pMHC-beads failed to enrich OVA_{257–264}-specific T cells (Fig. 6B, C). To validate the tumor-reactivity of the captured antigen-specific CD8⁺ T cells, we subjected captured T cells to an in vitro tumor-cell-killing assay against E.G7-OVA cells. Expectedly, T cells captured by pAPCs exerted superior tumor-killing activity across all the effector-to-target (E/T) ratios compared with non-enriched T cells and T cells captured by pMHC-beads (Fig. 6D). We did take notice that the overall enrichment efficiency for the endogenously induced SIINFEKL-peptide-specific T cells was lower compared to experimentation with OT-I T cells derived from transgenic

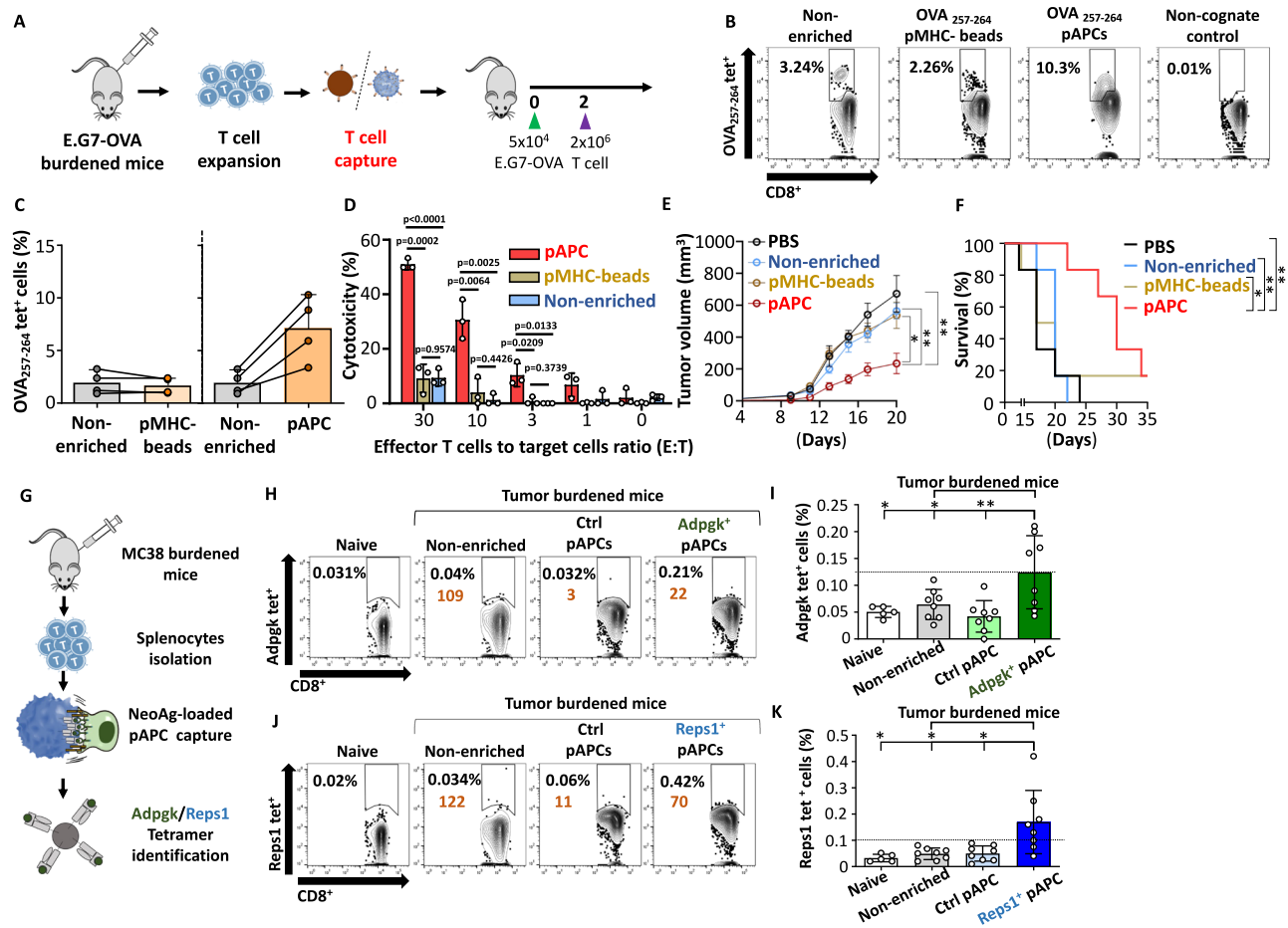


Fig. 6 | Tumor-reactive lymphocyte capture by pAPCs for adoptive cell therapy and neoantigen identification. **A** Schematic illustration showing the application of pAPC-mediated lymphocyte capture for improving adoptive T cell therapy. T cells were collected from E.G7-OVA burdened mice receiving ICB therapy, which were expanded for 7 days prior to antigen-specific T cell capture. After expansion, all the T cells underwent isolation by OVA_{257–264}-loaded pMHC-beads or pAPCs prior to adoptive cell therapy in a E.G7-OVA tumor challenge. **B** Representative flow cytometric scatter plot showing H-2Kb OVA_{257–264}-tetramer⁺ CD8⁺ T cells before and after lymphocyte isolation by either pMHC-beads or pAPCs. **C** Quantification of H-2Kb OVA_{257–264}-tetramer⁺ CD8⁺ T cells from 4 independent tumor burdened hosts before and after lymphocyte isolation with OVA_{257–264}-loaded pMHC-beads or pAPCs (Independent biological replicates $n = 4$). **D** Evaluation of in vitro tumor-killing capacity of T cells captured with pAPC, pMHC-beads, and non-enriched T cells against E.G7-OVA in various effector-to-target cells (E/T) ratio (Independent biological replicates $n = 3$). **E** Tumor growth following adoptive T cell therapy. Mice were inoculated with 5×10^4 E.G7-OVA and received 2×10^6 T cells on the following day. The error bars represent mean \pm standard error of the mean (SEM). P values from left to right, $*p = 0.0156$, $**p = 0.0023$, $**p = 0.0074$ ($n = 6$). **F** Tumor survival

curve from (E). Progression-free survival was defined as the time from 5×10^4 E.G7-OVA inoculation until the tumor volume exceeded 500 mm^3 . Gehan-Breslow-Wilcoxon test were performed. P value from left to right, $*p = 0.0349$, $**p = 0.0015$, $**p = 0.0017$. **G** Schematic illustration showing the application of pAPCs for capture and identification of neoantigen-specific T cells. T cells collected from MC38-burdened mice receiving ICB therapy underwent lymphocyte capture with Adpgk-loaded, Repl1-loaded pAPCs or control pAPCs with peptide loading. **H–K** The isolated cells were then stained with neoantigen-specific tetramers for analysis. Flow cytometric analysis of H2-Db Adpgk tetramer-positive T cells (**H**, **I**) and H2-Db Repl1 tetramer-positive T cells (**J**, **K**) among T cells pools following different preparation protocol. Dashed line indicates detection limit as determined by the average value of tetramer⁺ T cells from non-tumor-burdened mice plus 3 standard deviations. P values from (I) left to right, $*p = 0.0373$, $*p = 0.0374$, $**p = 0.0073$. P values from (K) left to right, $*p = 0.0302$, $*p = 0.0144$, $*p = 0.0163$ (Independent biological replicates $n = 5$ in naïve mice, $n = 8$ in the other groups). The error bars represent mean \pm standard deviation except in (E). Statistical analyses were performed by two-sided Student's t tests.

mice. This discrepancy was likely attributable to the lower average affinity of polyclonal, endogenously induced T cells in comparison to the monoclonal OT-I transgenic T cells. To demonstrate the utility of pAPC-based T cell isolation for enhancing adoptive T cell therapy, we compared non-enriched T cells, pMHC-beads-captured T cells, pAPC-captured T cells with similar functional state (Supplementary Fig. 7B) for adoptive transfer therapy against E.G7-OVA tumors. Mice administered with the pAPC-captured T cells exhibited enhanced tumor suppression as compared to the control treatment groups (Fig. 6E, F, Supplementary Fig. 7C), validating the enrichment of functional tumor-reactive T cells by the pAPC-mediated lymphocyte isolation. The encouraging result on tumor-reactive T cell isolation prompted us to further explore pAPC-based lymphocyte isolation for identifying

endogenous cancer neoantigen-specific T cells, the extreme scarcity of which can limit their detection⁴³. Adopting Adpgk and Repl1 neoantigens, which are two putative neoantigens identified from MC38 colorectal cancers through bioinformatics and mass spectroscopy⁴⁴, we examined whether lymphocytes responsive to these antigens could be identified from MC38-burdened mice followed by ICB treatment (Fig. 6G and Supplementary Fig. 8A). Consistent with prior findings that failed to detect Adpgk and Repl1-reactive T cells in an endogenous setting⁴⁵, tetramer staining with mice splenocytes showed no distinguishable signals for neoantigen-reactive T cells between control and tumor-burdened mice (Fig. 6H–K, Supplementary Fig. 8B). Contrastingly, after a single round of lymphocyte capture by pAPCs, Adpgk-pAPC- and Repl1-pAPC-enriched pools showed significantly elevated

and detectable signals for Adpgk-tetramer⁺ and Resp1-tetramer⁺ CD8⁺ T cells, respectively. As a control, lymphocytes captured with pAPCs without neoantigen peptide loading showed no elevation of tetramer⁺ T cells. These results corroborate pAPC's capacity to enrich lymphocytes even in low-frequency conditions, broadening its use in scavenging highly scarce neoantigen-reactive T cells.

Monoallelic pAPCs expressing HLA-A*02:01 enables isolation of virus- and tumor-specific T cells from human PBMCs and HLA-transgenic mice

Given that human leukocyte antigen (HLA)-expressing monoallelic APCs are a commonly adopted live cell probe strategy for clinically relevant antigen assessment^{46–48}, we further demonstrated the preparation of a monoallelic pAPC expressing HLA-A*02:01 using genetically modified HEK293T cells. HEK293T cells were edited by CRISPR to knock out their endogenous HLA alleles, and the cells were transfected with HLA-A*02:01 allele. The HLA-A*02:01 expressing HEK293T cells then underwent magnetization and intracellular polymerization for subsequent T cell capture (Fig. 7A). To isolate antigen-specific T cell from human donors, we acquired PBMCs from HLA-A*02:01-positive donors that were seropositive for cytomegalovirus (CMV). Using an immunodominant HLA-A*02:01-restricted CMV antigen pp65, we performed direct lymphocyte capture by pp65-loaded pHEK293T enriched pp65 tetramer-positive cells followed by a 15-min non-cognate dislodgement procedure (Supplementary Fig. 9A–C). Biomimetic lymphocyte capture by the antigen-loaded pAPC significantly enriched pp65 tetramer-positive T cells to ~32%, whereas control pAPCs without pp65 antigen loading showed no significant enrichment (Fig. 7B, C). To further demonstrate the monoallelic pAPC's applicability to capture therapeutically relevant tumor-reactive T cells, we inoculated HLA-transgenic mice expressing human HLA-A*02:01 with a melanoma-associated antigen MART-1 for subsequent capture and cytotoxicity assessment against C32 human melanoma cell line⁴⁹, which is known to express both MART-1 antigen and HLA-A*02:01 allele (Fig. 7D, Supplementary Fig. 10A). Examination of splenocytes from the inoculated mice showed that the vaccination yielded ~1.3% of MART-1 tetramer-positive T cells. Upon lymphocyte capture by MART-1-loaded pHEK293T, a 10-fold enrichment in MART-1 tetramer-positive T cells were observed (Fig. 7E, F, Supplementary Fig. 10B). In comparison to non-enriched T cells derived from the MART-1 antigen inoculated host, pAPC-captured T cells exhibited higher cytotoxic activity against C32 cells across various effector to target cell ratios (Fig. 7G). These results demonstrate adaptation of pAPCs for biomimetic capture and enrichment of clinically relevant virus- and tumor-reactive T cells.

Discussion

Recent demonstration of cellular polymerization through intracellular hydrogelation has shown new venues to enhance cellular functions and improve device performance through cell-gel hybridization, the facile transformation is universally applicable to a variety of cell lines as well as human primary immune cells, and has been shown to improve biomembrane research, feeder cell engineering, elevate the therapeutic probiotics designs, and development of biomimetic decoys against pathogenic molecules^{35–39,50}. The present work introduces a unique application of polymer-stabilized cells towards improving biomimetic lymphocyte capture. Our work shows that cellular polymerization addresses the fundamental challenge in live cell-based lymphocyte probes, which are susceptible to unpredictable antigen presentation that can influence probe specificity. The intracellular polymerization effectively preserves the morphology, membrane integrity, lipid order, and cell functionalities. The non-disruptive nature of the cytosolic polymerization retains key surface proteins of antigen-presenting cells (APCs), including MHC, CD80, CD86, and ICAM-1, enabling polymerized APCs (pAPCs) to undergo cell-like active engagement with cognate T cells and IS formation. Given the robustness and modularity of

polymerized cells, concentration kinetically driven peptide antigen replacement significantly resolves the stochastic antigen processing and uncertain presentation among live-cell platforms. Our kinetic pulsing technique leverages the stability of pAPCs to enable concentrated peptide pulsing in small volumes, which is conducive to peptide replacement and enables controlled and persistent antigen presentation for peptides of varying MHC affinities. Magnetization of pAPCs further permits label-free isolation of antigen-specific lymphocytes, providing a robust, cell-mimicking system that can improve the identification of endogenous antigen-specific T cells and adoptive cell therapy. Adaption of the pAPC system to clinically relevant settings is demonstrated with monoallelic HLA-A*02:01-expressing pAPCs, which show effective isolation of virus- and tumor-specific CD8⁺ T cells from human PBMCs and transgenic mice expressing HLA. With the growing interest in incorporating artificial materials to preserve or enhance biological functionalities of cellular systems^{39,51–53}, the present study presents a strategy to functionalize polymerized cells for therapeutic applications and offers insight on the interplay between living systems and synthetic materials.

The study also shows that the association time (on-rate) of non-cognate lymphocytes with pMHC-functionalized probes presents an underlying barrier towards discriminating rare T cell clonotypes. During APC engagement, T cell actively sample pMHCs to verify cognate antigens, and the process leads to a period of lymphocyte association time regardless of antigen-specificity⁵⁴. Although the on-rate of non-cognate lymphocytes is greatly lower than that of cognate lymphocytes, the influence of this temporary association on lymphocyte discrimination can be amplified as we show reduced cognate lymphocyte recovery in the presence of increasing non-cognate T cells. Allowing non-cognate lymphocytes to dislodge from the pAPCs before releasing the captured probes greatly enhances the enrichment fold of cognate lymphocytes. Future adoption of the pAPC system for antigen-specific lymphocyte identification can benefit from continuing incubation for antigen-specific T cell expansion following magnetic isolation^{17,52} as well as strategies to identify trogocytosis among isolated T cells. In addition, discrimination of T cell specificity may be further enhanced through the incorporation of fluidic systems that subjects engaged T cells to controlled shear stress^{19,55–57}. As the cytosolic polymerization strategy has been previously shown to facilitate conformal biomembrane functionalization of planar substrate³⁷, fluidic systems comprised of polymerized cellular monolayer with controllable and persistent antigen presentation can be envisioned.

Methods

Ethics statement

All experiments involving animals were conducted following experimental protocols approved by the Academia Sinica Institutional Animal Care and Utilization Committee, Academia Sinica, Taipei, Taiwan (#15-10-868). Mice were housed in individually ventilated cages under specific pathogen-free (SPF) conditions with a 12-h light/dark cycle (lights on at 07:00), at a controlled ambient temperature of 22 ± 2 °C and relative humidity of 50 ± 10%. The use of primary human cells was carried out under a protocol approved by the Institutional Review Board of Academia Sinica (AS-IRB01-23064). Gender was not considered in our experimental design.

Cell culture and preparation of monoallelic HLA-A*02:01-expressing HEK293T cells

JAWSII cells (ATCC, CRL-11904) were grown in alpha minimum essential medium (11095-080, Thermo Fisher Scientific, U.S.) supplemented with ribonucleosides, deoxyribonucleosides, 4 mM L-glutamine, 1 mM sodium pyruvate (11360070, Thermo Fisher Scientific, U.S.), 5 ng/mL murine granulocyte-macrophage colony-stimulating factor (GM-CSF) (315-03, PeproTech, Israel), and 20% fetal bovine serum (FBS) (315-010-CV, CORNING Inc., U.S.). For activation, 80% confluency of JAWSII cells in a 100 mm Petri dish were treated with 1 µg/mL of LPS for 20 h at

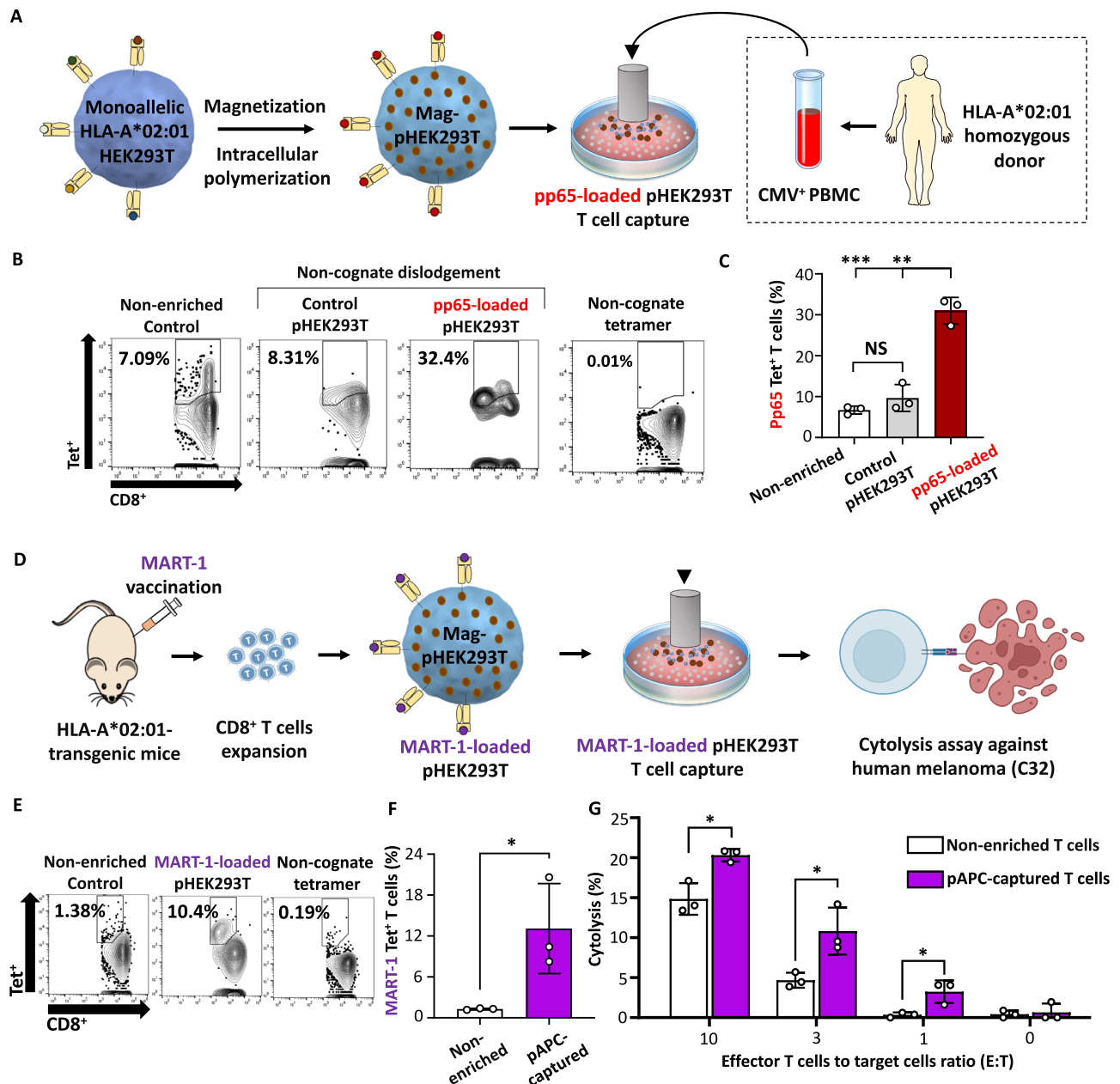


Fig. 7 | Human leukocyte antigen-specific T cells capture by monoallelic HLA-A*02:01-expressing pAPCs. **A** Schematic illustrating the preparation of monoallelic HLA-A*02:01-expressing pAPCs for subsequent capture of virus-specific T lymphocytes from human PBMCs. An immunodominant antigen of cytomegalovirus (CMV), pp65, was used for to capture virus-specific lymphocyte from 3 CMV⁺ donors. **B** Representative flow cytometric plots and **C** quantification of HLA-A*02:01-pp65 tetramer-positive T cells following different lymphocyte isolation protocols. Non-cognate T cell dislodgement was performed by suspending captured pAPCs in solution for 15 min. T cells capture with control pHEK293T without pp65 peptide loading was incorporated as a negative control. PBMCs from three individual CMV seropositive donors were conducted independently. *P* values, ****p* = 0.0002, ***p* = 0.0013, NS *p* = 0.2089. The error bars represent mean ± standard

deviation (*n* = 3). **D** Schematic illustration of MART-1-specific T cell capture and cytotoxicity evaluation against a human melanoma cell line. MART-1-specific T cells were induced via MART-1 peptide vaccination in HLA-A*02:01 transgenic mice. **E** Flow cytometric analysis and **F** quantification of HLA-A*02:01-MART-1 tetramer-positive T cells before and after capture with MART-1 loaded pHEK293T. *P* = 0.0363 (Independent biological replicates *n* = 3). **G** Cytotoxicity assessment of MART-1-loaded pAPC-captured T cells against C32 human melanoma cell line. 10⁴ C32 human melanoma cells were incubated with designated effector to target cell ratios (E:T) ranging from 0 to 10. Following 48 h of incubation, cytotoxicity was assessed using a LDH cytotoxicity assay. *P* value from left to right, **p* = 0.0113, **p* = 0.0257, **p* = 0.0252 (Independent biological replicates *n* = 3). The error bars represent mean ± standard deviation. Statistical analyses were performed by two-sided Student's *t* tests.

37 °C. For primary mouse T cell culture, RPMI1640 medium (10-040-CM, CORNING Inc., U.S.) was used and supplemented with 10% FBS, 1 mM sodium pyruvate, and 0.05 mM 2-Mercaptoethanol (2-ME) (M6250, MERCK, U.S.).

A Monoallelic HLA-A*02:01 expressing HEK293T cell line was prepared via genomic editing utilizing the CRISPR-Cas9 system. The process involved targeted deletion of endogenous HLA-A, HLA-B, and

HLA-C genes through co-transfection with specific single guide RNA (sgRNA) sequences: AGACCAACATCATCGGCGCGTCC (gRNA ID: g953), GGAGTGGCTCCGCAGATACCTGG (gRNA ID: g1455), GAGCC AGAGGATGGAGCCGCGGG (gRNA ID: gAE2), and GAAGGAG-AC GCTGCAGCGCACGG (gRNA ID: gAE3). This co-transfection was carried out with pLenti-hCas9-puro plasmid at a 1:3 ratio, resulting HLA-ABC null 293 T cells. The transfected cells were stained with

HLA-ABC antibody (HLA-APC-APC, G46-2.6, BD Bioscience, U.S.) to sort out HLA-ABC null cells in a fluorescence activated cell sorter. The sorted cells were then subjected to single clone culture for 3 weeks. Subsequently, all expanded clones were verified via PCR-based genotyping to validate endogenous HLA-ABC deletion using the indicated primers listed below: HLA-A forward primer: GAAACSGCCTCTGY GGGGAGAAGCAA, HLA-A reverse primer: TGTTGGTCCCAATTGTCT C-CCCTC, HLA-B forward primer: GGGAGGAGCGAGGGGACCSCAG, HLA-B reverse primer: GGAGGCCATCCCCGGCGACCTAT, HLA-C forward primer: CTCMTCCTGCT-GCTCTCGGGA, HLA-C reverse primer: TGGGAGGCCATCCCCGGGAGAT. Subsequently, the HLA-ABC null 293T cells were transduced with lentivirus carrying individual open reading frames (ORFs) of HLA-A02:01 and β 2 microglobulin. This strategic manipulation resulted in the creation of monoallelic HLA-A02:01-expressing HEK293T cells. During routine culture maintenance, a concentration of 10 μ g/mL puromycin was utilized to selectively enrich HLA-A02:01-expressing cells for subsequent T cell capture experiments.

Cell antigen pulsing and transfection

For the antigen presentation approaches, 6×10^5 of LPS activated JAWSII cells were treated with 48 μ g/mL ovalbumin, 3 μ g/mL OVA₂₄₈₋₂₇₄ long peptide (27 amino acids), 1 μ g/mL of SIINFEKL peptide for 4 h each to make sure they were pulsed with the same mole of the SIINFEKL. For transfection, live APCs were transfected using Maestrotectin Transfection Reagent according to the manufacture instructions (#MF002-1, Omics Bio, Taiwan) containing 3 μ g of SIINFEKL plasmid DNA for 48 h. Flow cytometric analysis was then performed on each group to characterize H2-Kb SIINFEKL⁺ cells.

Endotoxin detection

To characterize the levels of endotoxin in pAPCs or culture media, a gel clot-based assay kit (L00351, GenScript, U.S.) was utilized in this study. Lyophilized amebocyte lysate (LAL) derived from *Tachypleus tridentatus* was reconstituted in 2.2 mL of LAL Reagent Water. Subsequently, 0.1 mL of this reconstituted LAL reagent was co-incubated with each test group, including LPS as a positive control, in endotoxin-free tubes. After 1 h of incubation, gel clot formation in each group was observed. According to the manual instructions, clot formation indicated that the endotoxin concentration was above 0.25 EU/mL. Conversely, the absence of gel clot formation was verified as an endotoxin concentration below 0.25 EU/mL.

Transgenic mice & T cell isolation

C57BL/6-Tg (Tcratcrb) 1100Mjb/J OT-1 transgenic mice were kindly provided by Dr. Nan-Shih Liao from the Institute of Molecular Biology, Academia Sinica. Each breeding mouse underwent genome typing through gel electrophoresis analysis using 2X SuperRed MasterMix with loading dye (TE-SR01-10, BIOTOOLS Co., Ltd., Taipei, Taiwan). To obtain T cells from OT-1 transgenic mice, mice between 6 to 10 weeks old (gender was not considered) were sacrificed to acquire spleens, which were then strained using a sterile 40 μ m nylon cell strainer (#352340, BD Biosciences Falcon, U.S.) and incubated with 1 mL RBC lysis buffer (#555899, BD Biosciences, U.S.) for 2 min. OT-1 CD8⁺ T cells (CD8⁺ T cells specific for OVA₂₅₇₋₂₆₄ peptide restricted to H2-Kb) were isolated using the EasySepTM Mouse CD8⁺ T cell isolation Kit (Catalog #19853, STEMCELLTM technologies, Canada). The isolated CD8⁺ T cells were suspended in T cell medium for subsequent experiments. HLA-transgenic HLA-A02:01 mice were gifted by Dr. Shu-Wha Lin from the Department of Clinical Laboratory Sciences and Medical Biotechnology, National Taiwan University. The transgenic mice were generated by knocking out endogenous MHC alleles, including H-2K, H-2D, H-2L, from WT C57/B6 mice followed by homologous recombination with the human HLA-A02:01 allele.

HLA-transgenic mice (strain #003475) were obtained from the Jackson Laboratory for use in this study. These mice were generated via microinjection of the full-length human HLA-A2.1 gene into fertilized C57BL/6 eggs. The resulting Tg (HLA-A2.1)1Enge transgenic mice express high levels of the human class I MHC antigen HLA-A2.1 in splenic, bone marrow, and thymic cells. Genotyping of HLA-transgenic mice was performed using PCR with HLA-specific primers (Forward: 5'-TTCTCCCTC-TCCCAACCTATGTAG-3'; Reverse: 5'-CGACGACACTG ATTGGCTTCT-3').

Preparation and characterization of magnetic polymerized antigen-presenting cells

To confer magnetic properties to cells, 100 mg/mL of pegylated magnetic particles (MegaPro Biomdical Co., Ltd, Hsinchu, Taiwan) were incubated with 1×10^7 JAWSII cells for 24 h. Subsequently, the cells were activated with 1 μ g/mL LPS for 20 h. Following activation, the cells were harvested and resuspended as single cells in phenol-red-free α MEM medium (51200-038, Thermo Fisher Scientific, U.S.). They were then subjected to a 5-min incubation with 10 vol% isotonic poly(ethylene glycol) diacrylate Mn 575 (437441, MERCK, U.S.) supplemented with 0.5 mg/mL lithium phenyl-2,4,6-trimethylbenzoylphosphinate (LAP) (900889, MERCK, U.S.) for hydrogel and LAP infusion into cells. After the incubation period, the cells were centrifuged at $3000 \times g$ for 5 min. The supernatant was decanted, and the cells were suspended in phenol-red-free α MEM medium prior to photopolymerization at 365 nm light exposure for 1 min in a UV oven (UVP Crosslinker, Analytik Jena, U.S.). The resulting polymerized antigen-presenting cells (pAPCs) were isolated using the EasySepTM Magnet (#18000, STEMCELLTM technologies, Canada) to obtain magnetic polymerized dendritic cells. These isolated magnetic polymerized dendritic cells were then frozen in 10% sucrose at -80°C prior to lyophilization. The lyophilized pAPCs were stored at -20°C and reconstituted in water prior to experiments. Monoallelic HLA-A*02:01-expressing HEK293T-based pAPCs were prepared similarly, with the exception that the initial magnetic nanoparticle incubation lasted 48 h using 200 mg/mL nanoparticles.

To characterize the surface protein preservation on pAPCs, antibodies anti-MHC Class I (H-2Kb) (#17-5958-80, eBioscience, Thermo Fisher Scientific, U.S.), anti-OVA₂₅₇₋₂₆₄ (SIINFEKL) peptide bound to H-2Kb (#17-5743-80, eBioscience, Thermo Fisher Scientific, U.S.), anti-CD80 (B7-1) (#17-0801-82, eBioscience, Thermo Fisher Scientific, U.S.), anti-CD86 (#17-0862-82, eBioscience, Thermo Fisher Scientific, U.S.), and anti-CD54 (ICAM1) (#116105, BioLegend, U.S.) were applied to stain live APCs or pAPCs for flow cytometric analysis using Attune NxT flow cytometer (Thermo Fisher Scientific, U.S.).

Kinetically driven peptide loading and characterization of antigen presentation

To assess the peptide loading capacity of pAPCs, we conducted a titration experiment involving variations in both incubation time (ranging from 1 to 15 min) and concentration (ranging from 2^{-9} to 2^1 mg/mL) of OVA₂₅₇₋₂₆₄ peptide (SIINFEKL, BIOTOOLS Co., Ltd., Taipei, Taiwan) in 200 μ L water. This was aimed at replacing the original peptide located on the H-2kb molecules of pAPCs by driving kinetic-based peptide replacement. Subsequently, the binding kinetics of the newly loaded peptides were characterized using an anti-OVA₂₅₇₋₂₆₄ (SIINFEKL) peptide bound to H-2Kb antibody to validate replacement efficiency by quantifying H2-kb/SIINFEKL signal (%). Additionally, we employed other H-2kb-restricted epitopes, namely PB1₇₀₃₋₇₁₁ (SSYRRPVGI, AilBio, Taiwan) and E6-48 (EYDFAFRDL, Genscript, U.S.), to replace the OVA₂₅₇₋₂₆₄ peptide pre-loaded pAPCs. The efficiency of this replacement was evaluated by characterizing the binding of these peptides using the same anti-OVA₂₅₇₋₂₆₄ (SIINFEKL) peptide bound to H-2Kb antibody.

Nanoshell peptide vaccine preparation and mice vaccination

To induce a PBI₇₀₃₋₇₁₁-specific T cell response in vivo, we produced a peptide vaccine utilizing a poly(lactic-co-glycolic acid) (PLGA) based nanoshell through a water-oil-water double emulsion procedure⁵⁸. Initially, 20 μ L of an aqueous solution containing 4.5 mg/mL of PBI₇₀₃₋₇₁₁ peptide (SSYRRPVGI) and 1.5 mg/mL cdGMP (InvivoGen, U.S.) was emulsified in 200 μ L of a solution consisting of 75 mg/mL carboxyl-terminated 50:50 Poly(D,L-lactide-co-glycolide) (Mw 7000–17000) (#719897, MERCK, U.S.) in ethyl acetate. The emulsification process was conducted on ice using an Ultrasonic Probe Sonicator in pulse mode with 40% amplitude and on-off durations of 1 and 2 s for 1 min. The resulting first emulsion product was then added to 2 mL of 25 mM Tris-buffer and sonicated at 30% amplitude with on-off durations of 1 and 2 s for 2 min. The subsequently emulsified nanoparticles were poured into 8 mL of water at 40 °C for 1 h for solvent evaporation under gentle stirring. The PLGA nanoparticles were then concentrated and recovered using 100 kDa molecular weight cut-off Amicon filters (#UFC910024, MERCK, U.S.) to remove unencapsulated materials. To induce a MART-1-specific T cell response in HLA-transgenic mice, 20 μ L of an aqueous solution containing 4.5 mg/mL of MART-1 peptide (ELAGIGILTV) was encapsulated into a nanoshell peptide vaccine. The subsequent procedure for nanoshell preparation followed the same steps as described previously.

For mouse vaccination, female C57BL/6 or HLA-A02:01 mice between 6 and 8 weeks old were prepared for PBI₇₀₃₋₇₁₁ and MART-1 peptide vaccination, respectively. Each mouse received a subcutaneous injection of PLGA nanoparticles containing 30 μ g of PBI₇₀₃₋₇₁₁ or MART-1 peptide and 10 μ g of cdGMP. After 14 days, mice received a second vaccination to enhance their immune response. On day 21, all mice were sacrificed to collect splenocytes for subsequent analysis.

Functional assessment for pAPC antigen presentation

To validate peptide loading on pAPCs through a functional study, 10⁶ CD8⁺ T cells derived from OT-I transgenic or PBI-vaccinated mice were co-cultured with 2 \times 10⁵ pAPCs loaded either with SIINFEKL or SSYRRPVGI peptides in a 96-well U plate for 24 h. Subsequently, the cells were collected and stained with antibodies anti-CD8a (#17-0081-82, Thermo Fisher Scientific, U.S.) and anti-CD69 (12-0691-82, Thermo Fisher Scientific, U.S.) for flow cytometric analysis, aiming to investigate the extent of T cell activation.

Microscopic examination of immunological synapse formation

To examine T cell interaction with pAPCs under microscopy, 2 \times 10⁶ OT-I CD8⁺ T cells were cultured with 2 \times 10⁵ SIINFEKL-loaded pAPCs in a confocal dish (#200350, SPL Life Sciences, Korea) for 1 h. Prior to incubation, either T cells were pre-stained with antibodies anti-TCR V α 2 (#127805, BioVision, U.S.) and anti-LFA-1 (#141005, BioLegend, U.S.), or pAPCs were pre-stained with antibodies anti-MHC Class I (H-2Kb) and anti-CD54 (ICAM-1), respectively. Following incubation, samples were fixed with 4% paraformaldehyde for 10 min followed by 20 min with 10 μ g/mL of 4',6-diamidino-2-phenylindole (DAPI) (#28718-90-3, MERCK, U.S.) to visualize cellular nuclei, and analyzed with confocal microscopy.

For filamentous actin staining, pAPCs were stained with 25 μ M of CellTracker™ Blue CMAC dye (#C2110, Thermo Fisher Scientific, U.S.) for 45 min, while T cells were stained with 5 μ M of carboxyfluorescein succinimidyl ester (CFSE) (#150347-59-4, MERCK, U.S.) for 10 min. The two cell populations were then co-incubated for 1 h. After incubation, samples were treated with 4% paraformaldehyde for 10 min, permeabilized with 0.2% Triton X-100 for 20 min, followed by staining with 5 units/mL of rhodamine phalloidin (R415, Thermo Fisher Scientific, U.S.) for 40 min, and analyzed with confocal microscopy.

For T cell engagement frequency investigation, pAPCs were seeded on untreated 96-well black plate and polymerized or fixed using

2% glutaraldehyde solution. T cells and pAPCs were stained with anti-LFA1 (#141005, BioLegend, U.S.) and anti-CD54 (#116105, BioLegend, U.S.) antibodies respectively for 30 min at 37 °C. Wash three times with PBS and then resuspended T cells with T-cell culture medium. After co-incubating T cells with pAPCs, cell imaging was continuously recorded using high-content screening system (MD Image Xpress Micro XLS, Molecular Devices, U.S.) at 37 °C. Engagement event was analyzed using ImageJ.

Antigen-specific CD8⁺ T cell capture with pAPCs and pMHC-functionalized beads

To utilize pAPCs for antigen-specific T cell capture, 10⁶ total CD8⁺ T cells with either 10% or 0.1% OT-I CD8⁺ T cells were incubated with 10⁶ pAPCs loaded with SIINFEKL peptides or control pAPCs in a non-treated 24-well multidish (#144530, Thermo Fisher Scientific, U.S.). Where control pAPCs refer to pAPCs without kinetic-driven peptide replacement. For optimization of the incubation conditions, a protocol enabling T cell engagement was developed with various incubation densities ranging from 0.125 to 2 \times 10⁶ cells/cm² and various incubation times ranging from 0.5 to 36 h. To distinguish between OT-I and wild-type (WT) CD8⁺ T cells, WT CD8⁺ T cells were stained with 5 μ M of CFSE for 10 min prior to incubation with pAPCs.

Following incubation, a paraform-wrapped magnet was utilized to adsorb pAPCs and pAPC-engaged T cells. The collected cells were gently washed with PBS to remove any free or unbound T cells, after which the engaged T cells were separated by removing the magnet, and subsequently subjected to flow cytometric analysis to investigate the efficiency of antigen-specific T cell enrichment. For pMHC-coated Dynabeads capture, various densities of pMHCs ranging from 2 to 2 \times 10⁴ pMHCs/ μ m² of 5 \times 10⁷ pMHC-beads, which shared the same surface area as 10⁶ pAPCs, were subjected to T cell capture for 2 h. After incubation, the subsequent capture process was conducted using the same procedure as described above.

Trogocytosis assay

pAPCs were labeled with 20 μ g/mL of Alexa Fluor™ 647 NHS ester (Succinimidyl Ester) (#A20006, Thermo Fisher Scientific, U.S.) at room temperature for 1 h. Subsequently, the fluorescence-labeled pAPCs were incubated with 10⁶ OT-I or WT CD8⁺ T cells for 36 h to investigate T cell trogocytosis via H-2Kb or fluorescence transfer from pAPCs to cognate T cells. The cellular interaction was then stained with anti-mouse H-2Kb antibody (#116513, BioLegend, U.S.) and analyzed by flow cytometric analysis.

Preparation of pMHCs magnetic beads

An estimated 5 \times 10⁷ Dynabeads™ M-280 streptavidin (#1205D, Thermo Fisher Scientific, U.S.) were incubated with various quantities ranging from 2.5 \times 10⁹ to 2.5 \times 10¹³ of Flex-T™ biotin H-2KB OVA monomer (SIINFEKL) (#280051, BioLegend, U.S.) at room temperature for 1 h with gentle rotation. Following incubation, SIINFEKL-H-2KB-coated Dynabeads were washed and collected using a DynaMag™-2 Magnet (#12321D, Thermo Fisher Scientific, U.S.) for subsequent application in antigen-specific T cell capture. The input Dynabeads for T cell capture were determined by calculating the surface area equivalent to 10⁶ pAPCs. Biotinylated-SIINFEKL-H-2Kb monomer located on Dynabeads could be detected with anti-H2-kb-SIINFEKL antibody when the density exceeds 5 \times 10⁴ pMHCs/beads.

In parallel, to quantify the biotin H-2KB OVA monomer (SIINFEKL) conjugation efficiency, various numbers of input pMHCs ranging from a ratio of 0.005 to 50 \times 10⁴ pMHCs/beads were incubated using the same aforementioned procedure. Afterward, conjugated beads were removed and the supernatants were subjected to pMHC quantification using a micro BCA assay. The recovered pMHCs were determined by calculating the total input pMHCs minus the remnant pMHCs.

pMHCs conjugation and density calculation

To determine the precise number of pMHC molecules per bead, we used 2.8 μm Dynabeads™ M-280 Streptavidin, which have a calculated surface area of $24.61 \mu\text{m}^2$ ($4 \times \pi \times (1.4 \mu\text{m})^2$). The number of input pMHC molecules was estimated based on the total mass of pMHC divided by its molecular weight. For example, with an input of 5×10^4 pMHC molecules, the surface density was calculated as:

$$\frac{5 \times 10^4 \text{ pMHC}}{24.61 \mu\text{m}^2} \approx 2031 \text{ pMHC}/\mu\text{m}^2$$

For data presentation, this value was rounded to the nearest integer, yielding 2×10^3 pMHC/ μm^2 .

To compare with physiological conditions, we referenced the reported pMHC density of polymerized antigen-presenting cells (pAPCs), which varies between 0.5 and 3 million molecules per cell. We selected 2.5×10^6 pMHC molecules per cell as a reference point. Given an average pAPC surface area of $1256 \mu\text{m}^2$ ($4 \times \pi \times (10 \mu\text{m})^2$), the calculated density was:

$$\frac{2.5 \times 10^6 \text{ pMHC}}{1256 \mu\text{m}^2} \approx 2000 \text{ pMHC}/\mu\text{m}^2$$

Thus, 5×10^4 pMHC molecules per bead provided a comparable pMHC density for subsequent T-cell capture studies.

Isolation of endogenous antigen-reactive T cells

Eight-week-old female C57BL/6 mice were obtained from LASCO (BioLASCO Co., Ltd, Taiwan). To generate endogenous tumor-reactive T cells, each mouse was subcutaneously inoculated with 5×10^5 E.G7-OVA cells (BCRC, #60418) followed by three intraperitoneal injections of immune checkpoint blockade therapy (ICB) with 100 μg of anti-PD-1 antibodies (#BE0273, BioXcell, U.S.). Subsequently, these treated mice were sacrificed to collect CD8⁺ T cells for antigen-specific T cell capture by SIINFEKL-loaded pAPCs using the aforementioned optimized incubation conditions. H-2Kb OVA tetramer-SIINFEKL-APC (MBL Life Science Co., Ltd, Japan) was applied to characterize the enrichment efficiency by comparing the proportion of total CD8⁺ T cells before and after capture using flow cytometric analysis.

For MC38 endogenous neoantigen-specific T cell detection, 8-week-old female C57BL/6 mice were subcutaneously inoculated with 10^6 MC38 cells (Kerafast, ENH204-FP) followed by three intraperitoneal injections of immune checkpoint blockade therapy (ICB). Subsequently, these treated mice were sacrificed to collect CD8⁺ T cells for neoantigen-specific T cell capture by Adpgk, Reps1-loaded pAPCs or control pAPCs using the aforementioned optimized incubation conditions. Control pAPCs refer to pAPCs without kinetic-driven peptide replacement. H-2Db Adpgk neoepitope tetramer-ASMTNMELM or Reps1 neoepitope tetramer-AQLANDVVL (MBL Life Science Co., Ltd, Japan) were applied to characterize the proportion of neoantigen-specific T cells captured by pAPCs.

For MART-1 specific T cell capture, 8-week-old female HLA-A*02:01 mice were subcutaneously inoculated with MART-1 peptide vaccine on day 0 and 7. Subsequently, these treated mice were sacrificed to collect CD8⁺ T cells for MART-1 specific T cell capture by MART-1-loaded pHEK293T using the aforementioned optimized incubation conditions. HLA-A*02:01 MART-1 tetramer-ELAGIGILTV (MBL Life Science Co., Ltd, Japan) were applied to characterize the proportion of MART-1 specific T cell captured by pAPCs.

For pp65 specific T cell capture, PBMCs from CMV positive HLA-A*02:01-positive donors were collected for human CD8⁺ isolation by EasySep™ Human CD8⁺ T cell isolation Kit (Catalog #17953, STEM-CELLTM technologies, Canada). Subsequently, this human CD8⁺ T cells were captured by pp65-loaded pHEK293T or control pHEK293T using the aforementioned optimized incubation conditions. Control

pHEK293T refer to pAPCs without kinetic-driven peptide replacement. HLA-A*02:01 CMV pp65 tetramer-NLVPMTATV (MBL Life Science Co., Ltd, Japan) were applied to characterize the proportion of CMV pp65 specific T cell captured by pAPCs.

Ex vivo T cell expansion with T cell activator dynabeads

CD8⁺ T cells isolated from ICB-treated mice were subjected to ex vivo expansion at a concentration of 10^6 cells/mL using Dynabeads™ Mouse T-Activator CD3/CD28 (11452D, Thermo Fisher Scientific, U.S.) in Dulbecco's Modified Eagle's Medium (DMEM) (10-013-CM, Corning® Inc., U.S.) supplemented with 10% fetal bovine serum (FBS) and 30 U/mL recombinant interleukin-2 (rIL-2). When the density of T cells exceeded 2.5×10^6 cells/mL, the cultures were split back to a concentration of 0.5×10^6 cells/mL with replenished medium. After 7 days of expansion, the T cells were collected and subjected different T cell capture strategy prior to adoptive transfer therapy.

Tumor adoptive T cell transfer therapy

For adoptive T cell transfer therapy, 5×10^4 E.G7-OVA cells were inoculated subcutaneous on the right flank of C57BL/6 mice on day 0. Prior to adoptive cell therapy, the mice received an intravenous injection of 1 mg cyclophosphamide on day 1. On day 2, the mice were adoptively transferred with 2×10^6 CD8⁺ T cells derived from E.G7-OVA tumor-burdened mice described in the aforementioned protocol. The CD8⁺ T cells were either non-enriched, pMHC-beads captured, or pAPCs-captured. Tumor volume was monitored every 2–3 days and calculated using the formula: $(W^2 \times L)/2$, where W is the width and L is the length of the tumor.

Cell enrichment calculation

To analyze the efficiency of T cell capture with pAPCs or various ranges of pMHC-coated dynabeads, the recovered T cells were suspended in 1 mL of T cell culture medium, and 10 μL of the sample was subjected to a hemacytometer for direct T cell counting. Enrichment folds were determined by calculating the ratio of recovered OT-I/WT T cells over the input OT-I/WT ratio.

LDH cytotoxicity assay

10^4 of E.G7 OVA or C32 cells (BCRC, #60629) were seeded onto a 96-well plate and allowed to adhere for 16 h. The cells were then incubated for 48 h with designated T cells at varying effector T cells to target cell ratios, ranging from 0 to 30. After incubation, the plates were centrifuged at $300 \times g$ for 3 min, and 90 μL of the supernatant was collected. This was followed by the addition of 10 μL of LDH cytotoxicity assay reagent from the CytoSelect™ LDH Cytotoxicity Assay Kit (CBA-241, Cell Biolabs, Inc., U.S.). The reaction was allowed to proceed for 2.5 h, and absorbance was measured at 450 nm as the primary wavelength.

Statistical analyses

For statistical analyses, all experimental results were analyzed using either a two-sided Student's *t*-test or one-way analysis of variance (ANOVA) followed by Dunnett's multiple comparison tests, employing GraphPad Prism software. A *p* value smaller than 0.05 was considered significant, denoted as **p* < 0.05 and ***p* < 0.01.

Inclusion and ethics statement

This study was conducted in accordance with the principles of ethical research and inclusivity. All participants were treated with respect, and their rights and dignity were upheld throughout the research process. Informed consent was obtained from all participants prior to their involvement in the study.

Reporting summary

Further information on research design is available in the Nature Portfolio Reporting Summary linked to this article.

Data availability

All data supporting the present study is available in the manuscript, source data file, and supplementary information. Source data supporting the present study is available for Figs. 1–7, and Supplementary Figs. S1, S2, S4, S5, S6, S8, and S9. Source data are provided with this paper.

References

- Rosenberg, S. A. & Restifo, N. P. Adoptive cell transfer as personalized immunotherapy for human cancer. *Science* **348**, 62–68 (2015).
- Hont, A. B. et al. The generation and application of antigen-specific T cell therapies for cancer and viral-associated disease. *Mol. Ther.* **30**, 2130–2152 (2022).
- Li, S., Symonds, A. L., Miao, T., Sanderson, I. & Wang, P. Modulation of antigen-specific T-cells as immune therapy for chronic infectious diseases and cancer. *Front. Immunol.* **5**, 293 (2014).
- Waldman, A. D., Fritz, J. M. & Lenardo, M. J. A guide to cancer immunotherapy: from T cell basic science to clinical practice. *Nat. Rev. Immunol.* **20**, 651–668 (2020).
- Cheng, Y. et al. Non-terminally exhausted tumor-resident memory HBV-specific T cell responses correlate with relapse-free survival in hepatocellular carcinoma. *Immunity* **54**, 1825–1840.e1827 (2021).
- Moss, P. The T cell immune response against SARS-CoV-2. *Nat. Immunol.* **23**, 186–193 (2022).
- Chodon, T. et al. Adoptive transfer of MART-1 T-cell receptor transgenic lymphocytes and dendritic cell vaccination in patients with metastatic melanoma. *Clin. Cancer Res.* **20**, 2457–2465 (2014).
- Sibener, L. V. et al. Isolation of a structural mechanism for uncoupling T cell receptor signaling from peptide-MHC binding. *Cell* **174**, 672–687.e627 (2018).
- Bethune, M. T. et al. Isolation and characterization of NY-ESO-1-specific T cell receptors restricted on various MHC molecules. *Proc. Natl. Acad. Sci. USA* **115**, E10702–E10711 (2018).
- He, J. et al. Defined tumor antigen-specific T cells potentiate personalized TCR-T cell therapy and prediction of immunotherapy response. *Cell Res* **32**, 530–542 (2022).
- Foy, S. P. et al. Non-viral precision T cell receptor replacement for personalized cell therapy. *Nature* **615**, 687–696 (2023).
- Sewell, A. K. Why must T cells be cross-reactive? *Nat. Rev. Immunol.* **12**, 669–677 (2012).
- Stone, J. D., Chervin, A. S. & Kranz, D. M. T-cell receptor binding affinities and kinetics: impact on T-cell activity and specificity. *Immunology* **126**, 165–176 (2009).
- Corse, E., Gottschalk, R. A. & Allison, J. P. Strength of TCR-peptide/MHC interactions and in vivo T cell responses. *J. Immunol.* **186**, 5039–5045 (2011).
- Klenerman, P., Cerundolo, V. & Dunbar, P. R. Tracking T cells with tetramers: new tales from new tools. *Nat. Rev. Immunol.* **2**, 263–272 (2002).
- Mallajosyula, V. et al. CD8(+) T cells specific for conserved coronavirus epitopes correlate with milder disease in COVID-19 patients. *Sci Immunol* **6**, eabg5669 (2021).
- Hickey, J. W. et al. Efficient magnetic enrichment of antigen-specific T cells by engineering particle properties. *Biomaterials* **187**, 105–116 (2018).
- Bentzen, A. K. et al. Large-scale detection of antigen-specific T cells using peptide-MHC-I multimers labeled with DNA barcodes. *Nat. Biotechnol.* **34**, 1037–1045 (2016).
- Peng, S. et al. Sensitive detection and analysis of neoantigen-specific T cell populations from tumors and blood. *Cell Rep.* **28**, 2728–2738.e2727 (2019).
- George, A. J., Stark, J. & Chan, C. Understanding specificity and sensitivity of T-cell recognition. *Trends Immunol.* **26**, 653–659 (2005).
- Dolton, G. et al. More tricks with tetramers: a practical guide to staining T cells with peptide-MHC multimers. *Immunology* **146**, 11–22 (2015).
- Li, G. et al. T cell antigen discovery via trogocytosis. *Nat. Methods* **16**, 183–190 (2019).
- Wang, Y. et al. Deciphering membrane-protein interactions and high-throughput antigen identification with cell doublets. *Adv. Sci.* **11**, e2305750 (2024).
- Liu, Z. et al. Detecting tumor antigen-specific T cells via interaction-dependent fucosyl-biotinylation. *Cell* **183**, 1117–1133.e1119 (2020).
- Liu, H. et al. Antigen-specific T cell detection via photocatalytic proximity cell labeling (PhoXCELL). *J. Am. Chem. Soc.* **144**, 5517–5526 (2022).
- Joglekar, A. V. et al. T cell antigen discovery via signaling and antigen-presenting bifunctional receptors. *Nat. Methods* **16**, 191–198 (2019).
- Lee, M. N. & Meyerson, M. Antigen identification for HLA class I- and HLA class II-restricted T cell receptors using cytokine-capturing antigen-presenting cells. *Sci. Immunol.* **6**, eabf4001 (2021).
- Montealegre, S. & van Endert, P. M. Endocytic recycling of MHC class I molecules in non-professional antigen presenting and dendritic cells. *Front. Immunol.* **9**, 3098 (2018).
- van Endert, P. Intracellular recycling and cross-presentation by MHC class I molecules. *Immunol. Rev.* **272**, 80–96 (2016).
- Yewdell, J. W., Reits, E. & Neefjes, J. Making sense of mass destruction: quantitating MHC class I antigen presentation. *Nat. Rev. Immunol.* **3**, 952–961 (2003).
- Lanzavecchia, A., Iezzi, G. & Viola, A. From TCR engagement to T cell activation: a kinetic view of T cell behavior. *Cell* **96**, 1–4 (1999).
- McKeithan, T. W. Kinetic proofreading in T-cell receptor signal transduction. *Proc. Natl. Acad. Sci. USA* **92**, 5042–5046 (1995).
- Basu, R. & Huse, M. Mechanical communication at the immunological synapse. *Trends Cell Biol.* **27**, 241–254 (2017).
- Zhu, C., Chen, W., Lou, J., Rittase, W. & Li, K. Mechanosensing through immunoreceptors. *Nat. Immunol.* **20**, 1269–1278 (2019).
- Lin, J. C. et al. Intracellular hydrogelation preserves fluid and functional cell membrane interfaces for biological interactions. *Nat. Commun.* **10**, 1057 (2019).
- Lin, J. C. et al. Facile transformation of murine and human primary dendritic cells into robust and modular artificial antigen-presenting systems by intracellular hydrogelation. *Adv. Mater.* **33**, e2101190 (2021).
- Chien, C. Y. et al. In situ hydrogelation of cellular monolayers enables conformal biomembrane functionalization for xeno-free feeder substrate engineering. *Adv. Health Mater.* **12**, e2201708 (2023).
- Lin, C. L. et al. Rapid plasma membrane isolation via intracellular polymerization-mediated biomolecular confinement. *Acta Biomater.* **173**, 325–335 (2023).
- Contreras-Llano, L. E. et al. Engineering cyborg bacteria through intracellular hydrogelation. *Adv. Sci.* **10**, e2204175 (2023).
- Huppa, J. B. & Davis, M. M. T-cell-antigen recognition and the immunological synapse. *Nat. Rev. Immunol.* **3**, 973–983 (2003).
- Lanoix, J. et al. Comparison of the MHC I immunopeptidome repertoire of B-cell lymphoblasts using two isolation methods. *Proteomics* **18**, e1700251 (2018).
- Kuznetsov, A., Voronina, A., Govorun, V. & Arapidi, G. Critical review of existing MHC I immunopeptidome isolation methods. *Molecules* **25**, 5409 (2020).
- Vitiello, A. & Zanetti, M. Neoantigen prediction and the need for validation. *Nat. Biotechnol.* **35**, 815–817 (2017).
- Yadav, M. et al. Predicting immunogenic tumour mutations by combining mass spectrometry and exome sequencing. *Nature* **515**, 572–576 (2014).

45. Hos, B. J. et al. Identification of a neo-epitope dominating endogenous CD8 T cell responses to MC-38 colorectal cancer. *Oncoimmunology* **9**, 1673125 (2019).
46. Gurung, H. R. et al. Systematic discovery of neoepitope-HLA pairs for neoantigens shared among patients and tumor types. *Nat. Biotechnol.* **42**, 1107–1117 (2024).
47. Bruno, P. M. et al. High-throughput, targeted MHC class I immunopeptidomics using a functional genetics screening platform. *Nat. Biotechnol.* **41**, 980–992 (2023).
48. Weingarten-Gabbay, S. et al. Profiling SARS-CoV-2 HLA-I peptidome reveals T cell epitopes from out-of-frame ORFs. *Cell* **184**, 3962–3980.e3917 (2021).
49. Baulu, E., Gardett, C., Chuvain, N. & Depil, S. TCR-engineered T cell therapy in solid tumors: State of the art and perspectives. *Sci. Adv.* **9**, eadf3700 (2023).
50. Gao, C. et al. Targeted therapies of inflammatory diseases with intracellularly gelated macrophages in mice and rats. *Nat. Commun.* **15**, 328 (2024).
51. Baghdasaryan, O. et al. Synthetic control of living cells by intracellular polymerization. *Trends Biotechnol.* **42**, 241–252 (2024).
52. Macdougall, L. J. et al. Intracellular crowding by bio-orthogonal hydrogel formation induces reversible molecular stasis. *Adv. Mater.* **34**, e2202882 (2022).
53. McNally, D. L. et al. Reversible intracellular gelation of MCF10A cells enables programmable control over 3D spheroid growth. *Adv. Healthc. Mater.* **13**, e2302528 (2024).
54. Valitutti, S. The serial engagement model 17 years after: from TCR triggering to immunotherapy. *Front Immunol.* **3**, 272 (2012).
55. Descamps, L., Le Roy, D. & Deman, A. L. Microfluidic-based technologies for CTC isolation: a review of 10 years of intense efforts towards liquid biopsy. *Int J. Mol. Sci.* **23**, 1981 (2022).
56. Wang, Z. et al. Isolation of tumour-reactive lymphocytes from peripheral blood via microfluidic immunomagnetic cell sorting. *Nat. Biomed. Eng.* **7**, 1188–1203 (2023).
57. Ashby, J. F. et al. Microfluidic T cell selection by cellular avidity. *Adv. Health Mater.* **11**, e2200169 (2022).
58. Tsai, H. H. et al. Lymph node follicle-targeting STING agonist nanoshells enable single-shot M2e vaccination for broad and durable influenza protection. *Adv. Sci.* **10**, e2206521 (2023).

Acknowledgements

The authors acknowledge technical support for the confocal microscopy image acquisition from Show-Rong Ma, Common Equipment Core, Institute of Biomedical Science, Academia Sinica. Yao-Kuan Huang for the technical support on transmission electron microscopy from the Imaging Core Facility, Institute of Cellular and Organismic Biology, Academia Sinica. Dr. Dennis W. Hwang for providing the pegylated IOPs. The authors acknowledge funding support from Academia Sinica grant AS-GCP-113-L03 (C.M.J.H.), Ministry of Health and Welfare grant MOHW 113-TDU-B-222-134009 (C.M.J.H.), National Science and Technology Council grant NSTC 112-2628-B-001-014 (C.M.J.H.).

Author contributions

C.Y.H.: conceptualization, data curation, formal analysis, investigation, methodology, validation, writing-original draft, and writing-review and editing. P.C.T.: data curation and investigation. J.C.L.: data curation, formal analysis, and investigation. C.H.P.: data curation and investigation. Y.J.T.: data curation and investigation. B.Y.Y.: data curation and investigation. C.Y.F.: data curation and investigation. G.H.M.S.: data curation and investigation. L.C.W.L.: data curation and investigation. S.L.: data curation and investigation. H.C.Y.: methodology, supervision, and writing-review and editing. C.M.J.H.: methodology, project administration, resources, supervision, writing-original draft, and write-review and editing.

Competing interests

The authors declare no competing interests.

Additional information

Supplementary information The online version contains supplementary material available at <https://doi.org/10.1038/s41467-025-60321-3>.

Correspondence and requests for materials should be addressed to Hung-Chih Yang or Che-Ming Jack Hu.

Peer review information *Nature Communications* thanks Kwasi Adu-Berchie and the other, anonymous, reviewers for their contribution to the peer review of this work. A peer review file is available.

Reprints and permissions information is available at <http://www.nature.com/reprints>

Publisher's note Springer Nature remains neutral with regard to jurisdictional claims in published maps and institutional affiliations.

Open Access This article is licensed under a Creative Commons Attribution-NonCommercial-NoDerivatives 4.0 International License, which permits any non-commercial use, sharing, distribution and reproduction in any medium or format, as long as you give appropriate credit to the original author(s) and the source, provide a link to the Creative Commons licence, and indicate if you modified the licensed material. You do not have permission under this licence to share adapted material derived from this article or parts of it. The images or other third party material in this article are included in the article's Creative Commons licence, unless indicated otherwise in a credit line to the material. If material is not included in the article's Creative Commons licence and your intended use is not permitted by statutory regulation or exceeds the permitted use, you will need to obtain permission directly from the copyright holder. To view a copy of this licence, visit <http://creativecommons.org/licenses/by-nc-nd/4.0/>.

© The Author(s) 2025